This is to certify that the
thesis entitled

EFFECTS OF ARCH CAMBER AND BOUNDARY CONDITION ON
IMPACT-BASED ENERGY ABSORPTION

presented by

Peter John Schulz

has been accepted towards fulfillment
of the requirements for the

M.S. degree in Mechanical Engineering

Major Professor's Signature

August 25, 2006

Date

MSU is an Affirmative Action/Equal Opportunity Institution

EFFECTS OF ARCH CAMBER AND BOUNDARY CONDITION ON IMPACT-BASED ENERGY ABSORPTION

By

Peter John Schulz

A THESIS

Submitted to
Michigan State University
in partial fulfillment of the requirements
for the degree of

MASTER OF SCIENCE

Department of Mechanical Engineering

2006

ABSTRACT

EFFECTS OF ARCH CAMBER AND BOUNDARY CONDITION ON IMPACT-BASED ENERGY ABSORPTION

By

Peter John Schulz

Flat panels made of fiber composites have high energy absorption capability with low density when subjected to low-velocity impact. This thesis research focused on studying the effects of structural curvature on the composite's energy absorption ability. Arched composites with three curvatures were fabricated and centrally impacted at low velocities. Experimental results showed that the contact duration, the maximum deflection and the energy absorption increased as the arch camber increased while the stiffness and the peak load decreased. It was also found that the boundary condition played an important role in the energy absorption process. Three boundary conditions termed bar-clamped, frame-clamped and bolted were investigated. Bar-clamped specimens experienced the highest slippage with respect to the boundaries during central impacts followed by the frame-clamped ones. Bolted specimens had the least slippage and showed the most consistent results. The slippage of the boundaries in the specimens produced additional energy absorption.

DEDICATION

This work is dedicated to my wife Lisa and my parents for supporting me during my time in college.

ACKNOWLEDGEMENTS

Many thanks to my advisor Dr. Dahsin Liu for his guidance and teaching me to think creatively. I would also like to thank my committee members Dr. Alfred Loos and Dr. Patrick Kwon.

TABLE OF CONTENTS

LIST OF TABLES

LIST OF FIGURES

1. INTRODUCTION

Composite materials are a very effective form of vehicle armor due to their low density and high strength. Work at the Armor Research Lab [1] sought to show the effectiveness of glass-reinforced plastics compared to conventional steels. A fiber-reinforced epoxy composite is less dense than a conventional steel, but has a larger damage areas and less residual integrity. As a result armor systems with composites are designed in a patterned cellular design such that damage to one cell does not affect adjacent cells [2].

With the increasing demand for improved armor new designs must be tested. Typically laminated composites are reinforced in the z-direction to improve interlaminar strength [3]. Finding the most effective arrangement of the composite materials for energy absorption and weight reduction are desirable. Finding the most effective geometry and fiber angles for energy absorption are the goal. The arch is a common structural feature, which supports a structure, yet leaves space for an entryway into a building or decreases the amount of material needed in a bridge. It is unique in that stresses are distributed in plane. With the topological design of the arch and fiber angles a unique energy absorbing structure can be designed.

When designing a composite that absorbs the energy from an impact several parameters are typically considered. The strength to weight ratio is a measure of the composite strength compared to how much it weighs. Where the stiffness to weight ratio is a measures of the stress to strain ratio to the weight. The lightweight, high strength and stiffness are what make composites so lucrative compared to steals and other metals.

Some study has been done on arched laminated composites, but typically for measuring the impact response, characterize the damage, stress distribution, and buckling [4-18]. Work focusing on the energy absorption, curvature effects, and boundary conditions have not been widely studied. Damage characterization and buckling have been a focus of study, but give only some insight into what curvature and boundary conditions are best for armor.

1.1 Literature Survey

Understanding the failure phenomena of composite materials provides the key to energy absorption. Work by Kistler and Waas [12-14] has been done to characterize the response of arched composite panels due to impact. They showed that as the thickness decreases the curvature effects become more important. They concluded that flat panels respond to impacts with larger peak forces than the arched panels. Where the flat panel has a smaller maximum displacement. Kim, Im, and Yang [11] in a similar study mentioned that as the radius of curvature increases the contact force decreases. They also showed that a composite design with the smallest radius of curvature and the most interlaminar surfaces has the least amount of damage. As the panel becomes flat the impact force increases. Finite element work done by Zafer, et al. [16] shows this same trend, but he also mentions that with increasing curvature the maximum contact load will converge to a constant.

Work by Ambur, et al. [20] on the scaling effects of adjusting the ply-level or the sub-laminate in both flat and arched panels for non-linear impact response showed that the arched composites dissipate energy due to structural deformation and retain higher residual stiffness than a flat panel. In other work by Ambur, et al. [4] the contact force

initially increases as the radius of curvature becomes large. Eventually the contact force decreases as the radius of curvature continues to increase.

Baucom, Zikry, and Rajendran [22] said that in flat panels the main modes of energy dissipation are through delamination and matrix cracking, a stitched 3D woven fabric absorbs more energy than a 2D woven. Cheeseman and Bogettie [23] mentioned that the effects of wave propagation in a fabric during impact are an area of study. Woven fabrics are typically used to catch the projectile and spread the damage. A flat panel goes through a stiffening phase during impact. This is when the fibers are pulled taunt as the specimen bends. Kirkwood, et al. [24] mentions one of the energy modes is fiber pullout.

Eventually the layers will delaminate and many times fiber breakage will occur, both causing energy dissipation. Shenoi and Wang [18] studied the through-thickness stresses of arched composite laminates. Their work shows the maximum stress is on the inner side of the mid-plane. It would be deduced that failure would likely happen near the mid-plane first. The projectile geometry is also of significance where a blunt projectile shears the fibers. In most paper reviews a hemispherical design is used. In work by Hersberg and Weller [8] composite laminates with stitching were post-buckled and impacted. The critical load from the projectile decreased with increasing preloading. Stitching reduced the damage area caused by impact, whereas specimens in tensile load with stitching showed no change in the damage area.

Work by Short, Guild, and Pavier [19] on impact on arched composites showed a linear trend of damage area with increasing impact energy for a flat panel and two different radii. Ging, et al. [7] showed that low-speed drop impact tests in the transverse direction of cylinders with fibers angles at $\pm 55^{\circ}$ there was a non-linear trend overall in

the damage area with increasing impact energy after a certain energy level. The trend initially had a very sharp slope and after approximately 6J of energy the slope decreased dramatically.

Chun and Lam [5] worked on the modeling of three types of loading on arched panels, where the loading types are step, triangular, and explosive. They concluded analytically that the transverse deflection is mainly due to the impulses of the external loading, not to the peak of the load.

For an armor system a combination of ceramics and polymer matrix composites (PMC) would form a sandwich composite for ideal armor design [25-26]. Arched PMC would take the place or be added to conventional flat panel designs. A review of literature did not show arched composites in an armor system.

In summary of the literature mentioned on arched, cylindrical, and dome composites Table 1.1.1 was formed. It covers the testing type, analyses type, specimen geometry, radius of curvature, camber, length, thickness and the fiber angles. The analysis types ranged from low-velocity to quasi-static, with one studying using pressures at various frequencies. The analysis types were experimental and finite element modeling (FEM). The majority of the studies were done on ached composites. The boundary conditions were clamped for most of the studies, but some were clamped on the arched sides and others on the ends of the arches.

Table 1.1.1 Summary of literature on arched, cylindrical, or dome composites.

Reference No.	Primary Author	Year	Testing	Analysis Type	Specimen Geometry	Boundary Conditions	Radius of Curvature (mm)	Camber (mm)	Length (mm)	Thickness (mm)	Fiber Angles
4	Ambur, et al.	1998	Airgun Low-velocity	Exp.	Arch/Flat	Bolted	381-1524	-	127,229	1.016, 2.032	45,90
5	Chun, et al.	1995	Frequency w/ pressures	FEM	Arch	Clamped	-	-	-	-	0,30,90
6	Ciu, et al.	2004	Quasi-static	Exp./FEM	Dome	Clamped	100	-	-	1.9-4.2	0,45,90
7	Gning, et al.	2004	Low-velocity Quasi-static	Exp.	Cylinder	None	27.5	55	110	6	55
9	Huang, et al.	2004	Quasi-static	Exp./FEM	Arch/Flat	Slimply Supported	0-101	0-28.4		2.28	0,45,90
11	Kim, et al.	2004	Low-velocity	Exp.	Arched	Curved sides clamped	0-200	0-8.0	81	10	
12,13,14	Kistler, et al.	1994,1996,1999	Low-velocity	Exp./FEM	Arched	Clamped on curved and knife on straight	381-1524	1.4-3	254	1.02,2.03	0,45,90
15	Krishnamurthy, et al.	2001	Low-velocity	FEM	Arched	-	1.27m,2.54 m,25.4m	-	-	2.54	0,90
21	Spottswood, et al.	2001	Quasi-static	FEM	Arched	Clamped	152	-	102	0.804	0,45
29	Wardle	1998	Quasi-static	Exp./FEM	Arched	Clamped	152	-	102	0.804	0,45

1.2 Scope of Study

The scope of this study was two fold. One was to investigate the relationship between laminated composite curvature and energy absorption for low-velocity impact and the other to identify the effect of boundary condition on energy absorption. All specimens were made of the same pre-impregnated (prepreg) tape material and a cross-ply stacking sequence of $[0/90]_{3s}$ such that a comparison can be made between tests. Analysis of the load-deflection relation, the energy profile and the damage process were of primary interest as they provide the insight into the impact behavior of composites, such as peak load, deflection at the peak load, specimen stiffness, maximum specimen deflection, contact duration, energy absorption and damage modes.

1.2 Organization

The thesis is organized into nine chapters. Chapter 1 is an introduction of composite armor design and arched composites. Chapter 2 gives the details on the fabrication process, which consists of lamination of the prepreg tape, curing, and specimen preparation. Chapter 3 covers the equipment for testing, operating procedure, and data acquisition. Chapter 4 gives the details on the data analysis of the results obtained from the test procedure. Chapter 5 discusses the results from impact tests for specimens fixed on four sides versus two sides (plate vs. beam problem). The purpose was to show the boundary condition change from conventional clamping on four sides to only two sides clamped for flat panels. Chapter 6 is the analysis of the boundary condition and its effects on the impact on flat and arched composites clamped on two ends. Chapter 7 is the analysis of the effects of curvature on the energy absorption and impact behavior. Chapter 8 focuses on the buckling process of the arched composites. Additionally the

damage process for both the flat panel and arched composites are covered. Chapter 9 is the conclusions of this research study and recommendations for the future.

2. FABRICATION OF ARCHED SPECIMENS

The fabrication process consisted of layering prepreg (pre-impregnated) tape, molding the arched specimens, and curing the arched laminates in an autoclaving process. All arched specimens were fabricated from a glass/epoxy prepreg tape. They were twelve plies with a symmetric configuration to avoid any warpage due to unsymmetric thermal contraction after curing. To obtain the arched specimens, the composites were wrapped onto arched molds and cured in an autoclave. The other flat panels were cured in the autoclave as well as a hot press and are labeled in the appendecies.

2.1 Composite Material

The glass/epoxy prepreg tape is a product of Cymat [27] with an item number CYCOM 1003/W-490, but was formally a 3M™ product under the name Scotchply. The prepreg tape is a non-woven, unidirectional tape with continuous glass fibers along the length of the tape. The tape is in 30.48cm (12") wide rolls at 65.8m (72 yards) per roll. The glass is an electrical grade, i.e. E-glass. The tape was sealed inside a large Ziploc™ bag and stored in a freezer. It was removed from the freezer approximately 45-60 minutes prior to use to prevent condensate buildup on the tape, to allow flexibility, and to prevent it from un-sticking from the wax paper backing before stacking with the other layers.

2.2 Manufacturing Procedures

A conventional stacking sequence of $[0/90]_{3s}$ was chosen for this study. In manufacturing, the prepreg tape was first cut into 30.48cmx30.48cm (12"x12") layers. For flat panels, twelve layers of tape were stacked into a 30.48cmx30.48cm (12"x12") laminate. For arched specimens, the uncured laminate was further cut into 6.99cm (2.75") wide strips. The strips were then trimmed to desired lengths such that they could

be wrapped onto molds without any excess. For the small arch, the strip length was 12.7cm (5.0"), the medium arch 13.34cm (5.25"), and the large arch 13.97cm (5.5"). Figure 2.1.1 shows the dimensions of each arch. It can be seen in Figure 2.1.1(a) that the span of each arch is maintained at 7.62cm (3.0"). The thickness is also maintained at 0.249cm (0.098"). The "wings" on either side are maintained at 2.54cm (1.0"). The width dimensions of the specimens can be seen in Figure 2.1.1(b), where it is maintained at 6.99cm (2.75"). The other dimensions of the arches, camber (y) or arch height, radius of curvature (r), curvature (1/r) or inverse of the radius, and arc length can be seen in Table 2.1.1. The arc length does not include the "wing" portions, just the curvature. The composite strips are cut with an extra 50.8mcm (2.0") added to the arch length to account of the winged portion.

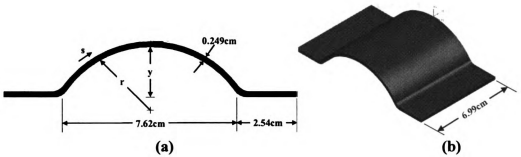

Figure 2.1.1 (a) Schematic of end view of arched composite with dimensions, (b) Schematic of arched composite showing the width.

Table 2.1.1 Arch and mold dimensions

Mold Type	Camber (y), mm (in.)	Radius (r), mm (in.)	Curvature (1/r), mm (in.)	Arc Length (s), mm (in.)
Small	7.95 (0.313)	84.14 (3.31)	0.0119 (.302)	76.2 (3.0)
Medium	15.88 (0.625)	57.15 (2.25)	0.0175 (.444)	83.82 (3.3)
Large	20.65 (0.813)	44.45 (1.75)	0.0225 (0.571)	88.9 (3.5)

The molds were fabricated out of steel pipe cut lengthwise and welded to a steel plate. Figure 2.1.2 shows a schematic one of the three steel molds. A typical mold could hold up to three composite strips. Each composite strip was wrapped onto the arched portion and onto the flat portion such that each arched specimen had 2.54cm (1") "wings" on either side. The composite wings were taped to the mold with masking tape to prevent them from sliding during autoclaving.

Figure 2.1.2 Steel mold schematic of pipe cut lengthwise on a plate.

The arched portions of the molds varied in length from 22.86cm to 27.98cm (9" to 11"). The steel pipes were cut parallel to the axis such that the maximum span of the curvature was maintained at 7.62cm (3.0"). The steel plates dimensions were 30.48cmx12.7cmx0.635cm (12"x5"x0.25"). Table 2.1.1 shows the major dimensions of the composite strips made from these molds.

2.3 Curing Process

The composite laminates and strips were cut to size prior to curing, sealed inside Ziploc™ bags and kept in the freezer. Prior to autoclaving, the bagged laminated

prepreg strips were removed from the freezer and given 30-45minutes to warm up. The molds were previously wrapped with non-stick release films and the support plate for the seven molds was covered in two layers of bleeder cloth (details given below). Once the composites were warmed up, they were pressed onto the molds and further wrapped with non-stick release materials.

Figure 2.1.2 shows seven molds without any of the release materials, bleeder cloth or vacuum bag. The diagram shows the location of the molds, composite strips, and the foot valve for pulling vacuum. The foot valve was located in the valley of two specimens. Each mold was covered individually with release materials and all seven molds covered on top and bottom with bleeder cloth.

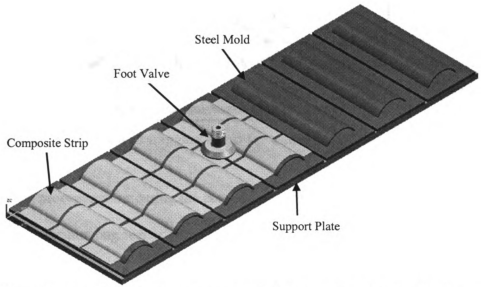

Figure 2.1.3 Mold setup with composite strips and foot valve location.

A end view diagram of the bagging materials used for the molding setup can be seen in Figure 2.1.3. To preventing sticking, each steel mold was covered in non-porous Teflon sheets. A pours layer was then laid to aid in release of the specimens after curing. Next, the uncured composite strip was pressed onto the mold and the wing ends taped to

prevent movement. The composite strips were then covered in a layer of porous Teflon and a layer of non-porous Telfon. Two layers of bleeder cloth were laid underneath all the molds on the support plate and two layers of bleeder cloth were placed on top of all the wrapped molds. An extra thick piece of bleeder was inserted directly below the foot valve to prevent epoxy from being sucked into the valve and to provide a cushion between the valve and the composite below.

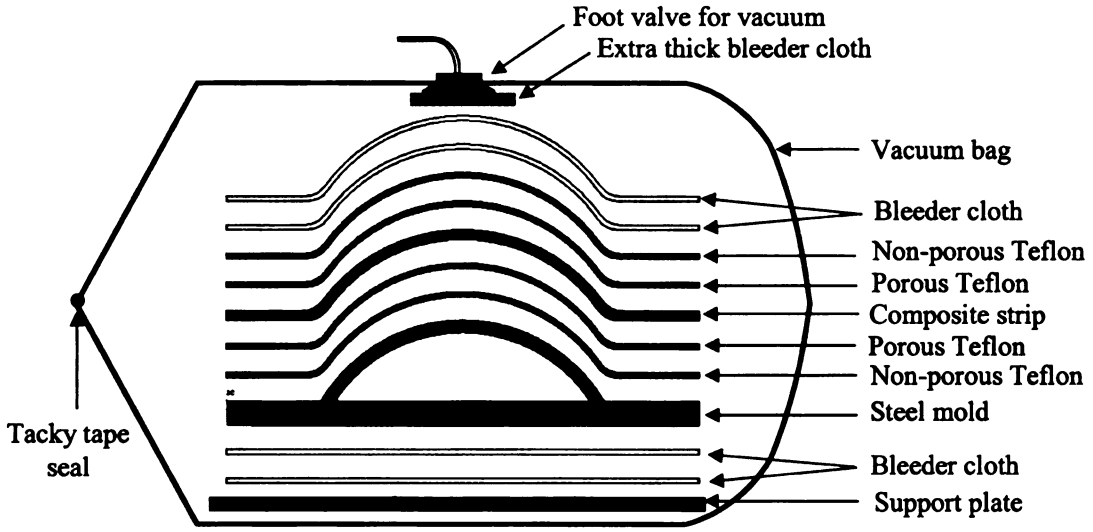

Figure 2.1.4 Side view of bagging setup for autoclave curing.

The process procedures for curing the composites in the autoclave are as follows:

1) Check vacuum bag seal.
2) Close autoclave and pressurize to 551kPa (80psi).
3) Temperature begins ramping from ambient to 160°C (320°F) at a rate of 5°C/min (10°F/minute).
4) When the temperature reaches 121°C (250°F), the vacuum is shut off and the vacuum vent opens. The pressure of 551kPa (80psi) is maintained.

5) Once the 160°C (320°F) temperature is reached, it is maintained for 45 minutes.

6) The last stage is cooling where the temperature decreases at a rate of 5°C/min (10°F/minute) to 26.7°C (80°F), at which time the pressure is released.

Note: The flat panels cured in the hot press underwent the same pressures and temperature cycles.

After the composite arches were cured, the bagging, Teflon, and bleeder cloth were removed along with the cured composites. Sometimes the epoxy bridged the specimens, bonding them together. The specimens were cut to separate the specimens. The specimens were then numbered and the centers were marked.

2.4 Specimen Preparation

The impact location at the peak of the arch was identified by tracing the specimen curvature onto graph paper. The peak of the trace on paper was found by sweeping two arcs with centers at the ends of the "wings" with a compass. The arch peak was located by the intersection of these arcs. The arched composite was then laid back onto the trace and the peak was marked on the specimen. Then the middle of the specimen was found by measuring half of the axial length of the specimen.

Each specimen was labeled according to the curvature, the fiber angles, and a specimen number or letter. For example, there were three curvatures named small, medium, and large, where the first letter S, M, or L designated the curvature. The fiber angles being $[0/90]_{3s}$, thus the name would include 090. An example specimen name would be M090-A. This would represent the first specimen in a series of medium arches with $[0/90]_{3s}$ stacking sequence.

Three boundary conditions named bar clamped, frame clamped and bolted were involved in the study. The specimens with the bolted boundary condition required an extra step in preparation. The holes are drilled slightly larger than 6.35mm (0.25") at 3.81cm (1.5") apart and centered on the wing. Each specimen was set underneath the clamping frame and a drill press was used to drill holes into the specimen through the holes in the frame.

3. TESTING

All specimens were tested using a modified low-velocity instrumented drop-weight impact system from Dynatup [28]. The impact results produced the impact velocity and the load history in terms of voltage. The histories of impact load (in terms of N or lbs), deflection, velocity, and absorbed energy were obtained subsequently with the use of a computer program based on Newton's second law and mathematical integration. Calculation was also done to determine the impact energy so that a comparison could be made with the absorbed energy. Each test was run under the same conditions and setup to eliminate additional variables beyond adjusting the impact energy. The following sections will give details on the equipment and standard operating procedures.

3.1 Testing Equipment

3.1.1 Low-velocity drop-weight impact test

A schematic for discussion purposes of the low-velocity impact test setup can be seen in Figure 1.1.1. Starting at the top, there are several important features to note. First, there is the crosshead, which has a load cell tup and two flags. It is attached to a rail clamp. The load cell has a 22241N (5000lb$_f$) capacity and a 12.7mm (0.5") hardened steel hemispherical tip for impacting the specimen. Assumed to be perfectly rigid, the load cell measures the load during impact. The two flags run through the infrared detector right before impact to record the impact velocity at the moment of contact between the specimen and tup tip. The velocity obtained by dividing the distance between the flags with the time it takes the flags to run through the detector. The rail clamp allows adjustment of the height of the crosshead on the guide rails. The latch is pressed to release the crosshead from the rail clamp.

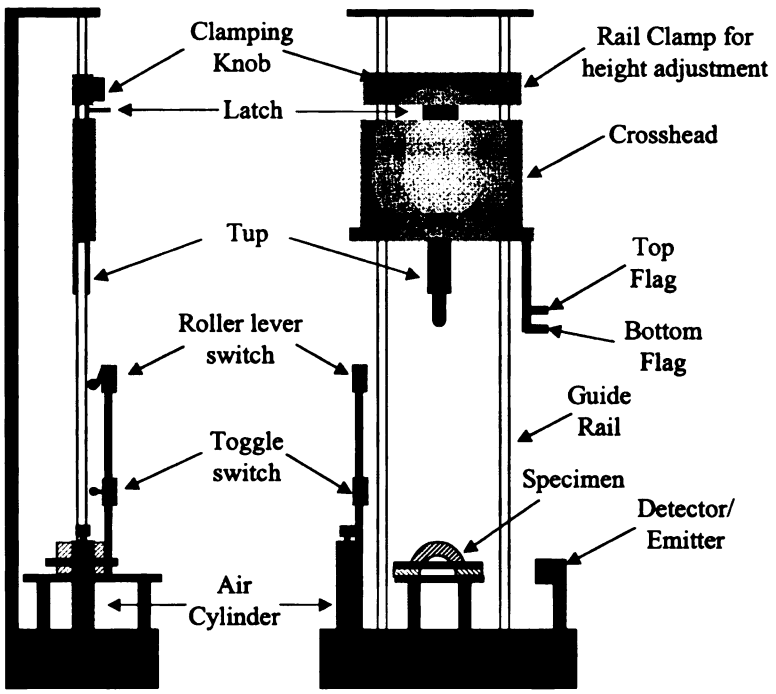

Figure 3.1.1 Side and front view schematic of impact testing.

The specimen is clamped at the base of the equipment such that the tup tip impacts the center of the specimen. If the impact energy is low enough, the crosshead/tup will rebound several times, further damaging the specimen. To prevent this, a rebounding system is in place. The crosshead will cause the toggle switch to go from an off (central position) to an on (downward) state at impact. Since the distance between the switches is greater than that of the crosshead height, the roller lever switch will remain off (outward) during impact. If the crosshead rebounds away from the specimen, it will leave the toggle switch in an on (downward) position and depress the roller lever switch into an on (inward) state. The roller lever switch is a momentary spring loaded switch such that it is naturally in an off state unless the top or bottom of the crosshead is pressing the lever to an on mode. The switches are in series, thus if both are in the on position, a solenoid

valve will activate the air cylinder upwards which prevents the tup from touching the specimen again.

To control the amount of impact energy, either deadweight can be added to the crosshead or the crosshead height can be changed. This allows duplication of the tests. The crosshead height is determined by measuring the distance from the tup tip to the impact location on the specimen. The total impact weight (crosshead, tup, flags and deadweight) is recorded so that accurate impact energies can be calculated.

3.1.2 Low-velocity impact data

When impact takes place, the load cell records the tup load, *F(t)*. To find the acceleration, Equation (3.1) is used, where the tup load is divided by the the total impact mass, *m*. The data is recorded every 25μs.

$$a(t) = F(t)/m. \tag{3.1}$$

From the acceleration calculation in Equation (3.1), the velocity of the tup can be determined. Equation (3.2) is the numerical integration of the acceleration over time. Since the tup is decelerating during the impact, the integration is multiplied by –1. The initial velocity v_i is determined by the infrared detector and is added to this integration.

$$v(t) = -\int_0^t a(t)dt + v_i \tag{3.2}$$

Equation (3.3) shows the final calculation to determine the deflection of the specimen during impact. The velocity is integrated over time from zero to the final time of the impact.

$$\delta(t) = \int_0^t v(t)dt \tag{3.3}$$

The data acquisition program also calculated the absorbed energy. However, due to important subtleties in calculating the absorbed energy by the specimen, the calculations will be covered in the chapter on data analysis.

3.2 Operating Procedure

3.2.1 Pre-impact test adjustments

Before running the first test, several adjustments were made to the impact testing machine. Initially, the specimens were prepared by marking the centers and drilling holes in the ends if they were bolted instead of clamped. A specimen was then fixed into the clamping system such that it was centered. Any weights in the crosshead were removed and the crosshead lowered by hand until the tup tip touched the impact location of the specimen. While the tup tip was resting on the specimen, the infrared sensor was adjusted up or down such that the second leading edge of the bottom flag is about 3.2mm (0.125") beyond the centerline of the plastic insert in the detector block. This adjustment assured that the velocity at impact was recorded. The toggle switch was adjusted such that the crosshead pushed it from its originally off (central) position to an on (downward) position just before impact. The distance between the toggle switch and roller lever switch was checked so that the roller lever switch was not being depressed to its on (inward) at the same instant the toggle switch was being pushed into an on (downward) position, thus prematurely activating the rebounding system at impact.

3.2.2 Impact test procedure

Once the pre-impact adjustments were done testing could begin. The specimen was centered on the clamping fixture and clamped (or bolted). Weights were added to the crosshead if needed and the crosshead height adjusted. The computer was set to retrieve the data from the load cell and infrared sensor. A personnel protection shield was set in place and the latch pressed to release the crosshead tup, allowing gravity to accelerate it toward the specimen.

3.2.3 Rebounding and perforation

For convenience it was desirable to find a particular weight to run all tests and only adjust the height when changing the impact energy. For this reason, a particular weight that caused both perforation and rebounding at different heights was determined in the first couple of tests. To accomplish this, several weights were loaded into the crosshead, typically in 2.27kg (5lbm) increments. The crosshead was adjusted to the maximum height to determine if perforation was possible at this maximum height. If perforation was reached, the height was decreased until rebounding occurred for following specimens.

Each new test involved a new undamaged specimen. Specimens were never impacted twice. However, occasionally multiple impacts occurred due to the rebounding system not activating. Specimens with multiple impacts are noted in the appendices.

3.2.3 Data Acquisition

The voltage signals from the load cell and infrared sensor are sent to a computer data acquisition unit. The computer obtains the load and impact velocity. The results are obtained at a rate of 25μs up to 100ms. The computer outputs the load, deflection,

velocity, and absorbed energy for each time step. This data is sent to a print file for conversion to an Excel™ spreadsheet.

4. DATA ANALYSIS

The most fundamental data from the impact experiments performed in this thesis research was impact force recorded in voltage. The experiments resembled impact forces due to a projectile, shock wave, crash or combination of them. The fundamental data could be converted into force (N or lb_f), acceleration, velocity, displacement, and energy histories. To protect against the impact force, armor composites must absorb the associated impact energy so that it is not transferred to the combat personnel and vehicle equipment. In understanding how energy is absorbed, the load-deflection relation and the energy profile play are important keys.

4.1 Load-Deflection Relation

The load-deflection relation is the most fundamental way to describe behavior of composites during impact. A load-deflection relation can be established by plotting the force against the corresponding displacement throughout the entire impact event. It provides the majority of data for impact analysis. This relation can also give insight to how a composite damages. Most important, it shows how the composite absorbs the impact energy throughout the impact process.

There are two general types of load-deflection curves based on whether or not the tup tip penetrates the specimen or rebounds. Figure 4.1.1 shows these two types of curves for a frame clamped flat panel and a bolted medium arched panel, where the closed curves are rebounding and the open curves are penetration. For the closed curves, notice how the load increases to a peak load and loops back to the start such that the load decreases as the deflection also decreases. This looping back of the curve is due to the crosshead/tup rebounding upwards, which causes the load to decrease and as the

specimen deflects back. Penetration takes place as the tip embeds into the specimen. Once penetration is reached, there is no rebounding of crosshead and tup, resulting in an open curve. When the tup tip punches through the specimen, it is defined to be perforation. Once perforation is reached, there is still a small load due to the tup tip rubbing on the specimen. Since the specimen has been perforated, this small load is not considered in the energy absorption calculation.

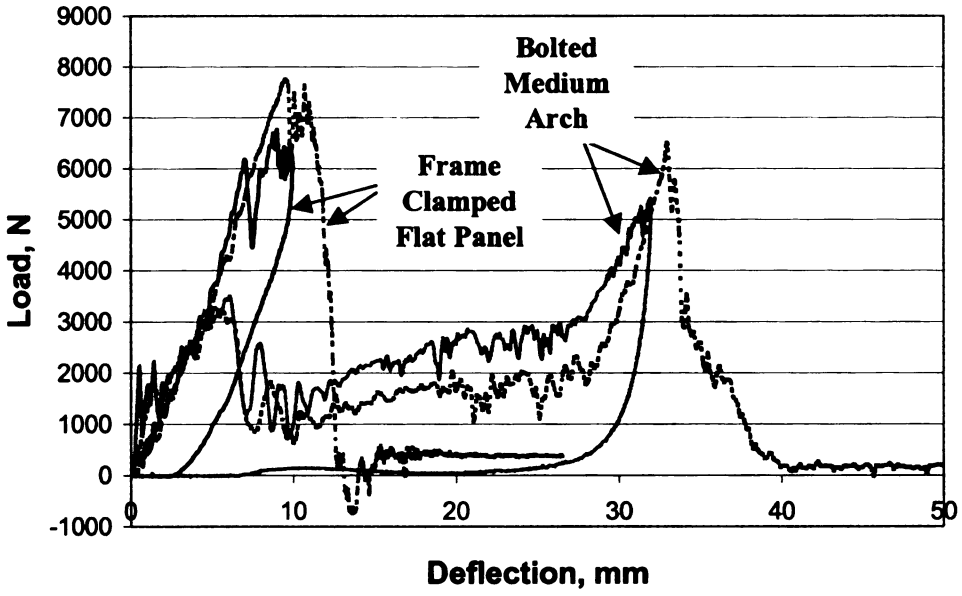

Figure 4.1.1 Load-deflection curves for frame clamped flat panel and bolted medium arch.

The load-deflection curves for different impact energies for a particular design are typically plotted on one chart. Figure 4.1.2 shows such a chart for a flat panel with the ends bolted to the testing fixture. Notice that the curves follow a pattern for the rise in load, which reaches a maximum near 6,800N. The maximum deflections are on average about 15mm. There are three closed curves and three open curves.

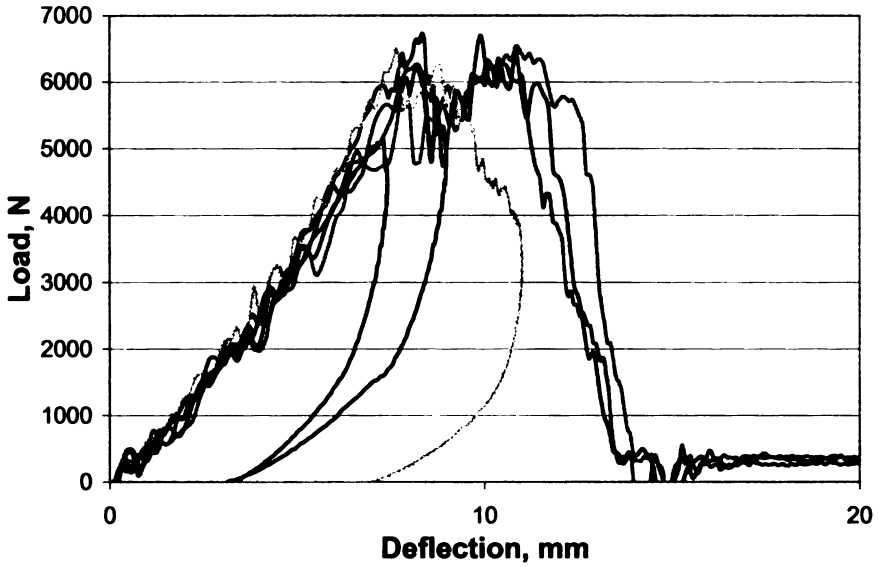

Figure 4.1.2 Load-deflection curves of bolted flat panels.

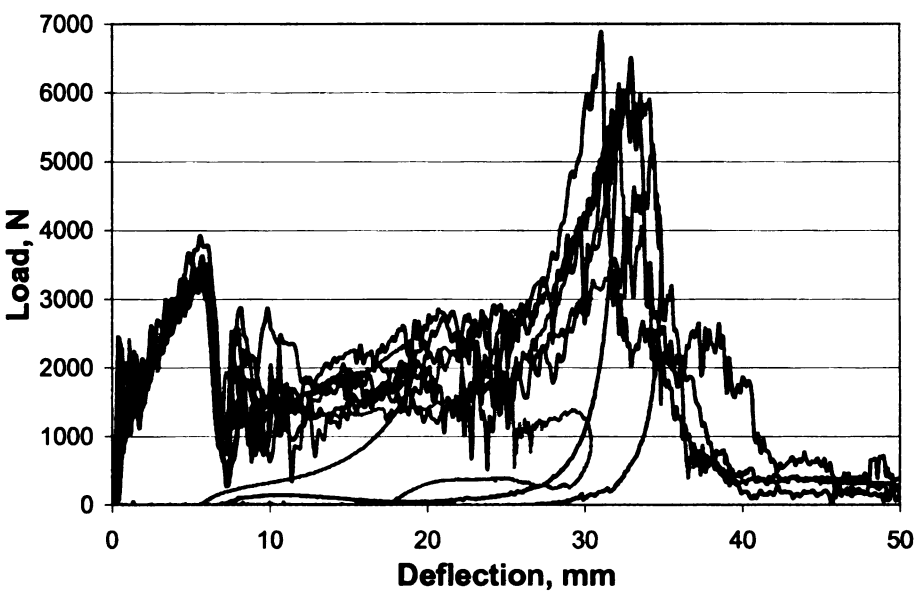

Figure 4.1.3 Load-deflection curves of bolted medium arch.

In comparison, the load-deflection relation for bolted medium arched specimens can be seen in Figure 4.1.3. The shape of the curves has changed dramatically. There are two peaks and a much larger maximum deflection. The maximum loads are

approximately just over 6,000N and the maximum deflection around 40-47mm. There are four closed curves and four open curves.

The energy absorbed by the composite during impact is calculated via Equations (4.1.1) and (4.1.2). It is simply the determination of the area bounded by the load-deflection curves. The load $f(\delta)$ defined in Equation (4.1.1) is integrated over the deflection δ. The upper limit δ_t is taken as the final deflection for closed curves. For the open curves, the limit δ_t is determined by the extension method, which is explained in the next section.

$$F = f(\delta) \tag{4.1.1}$$

$$E_a = \int_0^{\delta_t} f(\delta) d\delta \tag{4.1.2}$$

4.1.1 Extension Method

Determining the area for integration on the open load-deflection curves is critical for determining accurate energy absorption. Figures 4.1.4 is for a frame clamped flat panel and Figure 4.1.5 for a bolted medium arch. They show plots with open curves where perforation takes place. A line is extended to the abscissa at the same slope as the descent of the load during the penetration process. This line is the extension of the load-deflection curve to eliminate the effects of the friction due to the rubbing of the tup with the specimen after perforation. The location where the extension intersects the abscissa is the upper bound, δ_t in Equation (4.1.2).

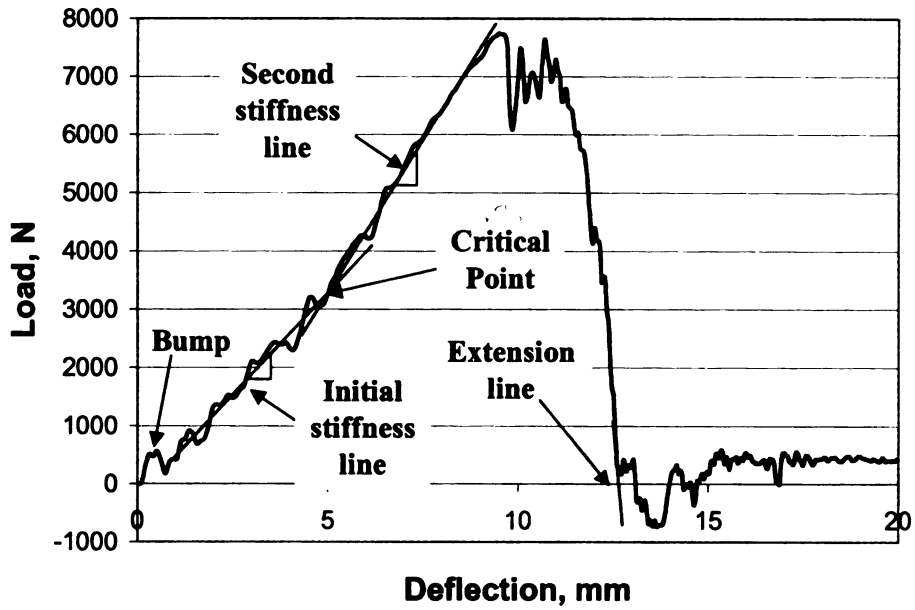

Figure 4.1.2 Load-deflection curve of frame clamped flat panel

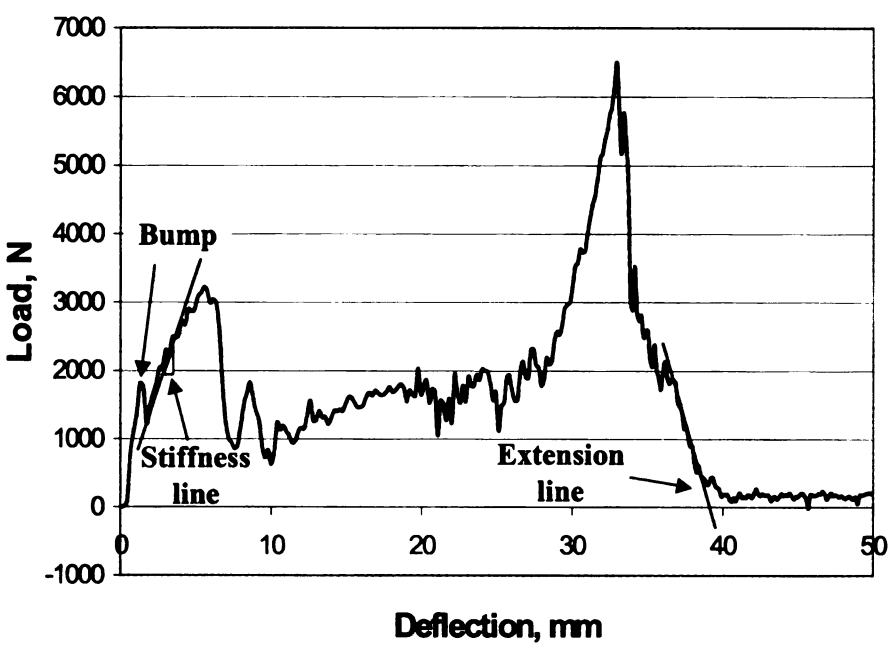

Figure 4.1.3 Load-deflection curve of bolted medium arch.

4.1.2 Impact Stiffness

The stiffness can be divided into two parts for a flat panel. The initial stiffness is determined by obtaining the slope during the initial major rise a load-deflection curve as

seen in Figure 4.1.4 and Figure 4.1.5. There is a bump in the load in both plots. This small bump is not included in the determination of the stiffness (slope). For the arched composites, this bump in the load-deflection curve is much more pronounced, as shown in Figure 4.1.5 and again is not included in the structural stiffness. Also notice how the slope of the initial stiffness changes for the flat panels into the second stiffness at a deflection around 5.0mm in Figure 4.1.4. The critical point in this stiffness change is believed to be the onset of delamination. This stiffness change is not as apparent for the arched composites.

4.1.3 Peak Load

The peak impact load changes based on specimen curvature and clamping boundary condition. A flat panel produces a single peak load, where the load increases sharply and then drops sharply with a relatively small deflection. An arched composite, however, produces different peak loads depending on the clamping boundary condition. If the specimen is clamped, there will be a single peak load amongst many oscillations. An arched specimen that is bolted will produce two peak loads, where the initial peak load is much smaller than the second peak load. The second peak load for arched composites is comparable to the single peak of the flat panel.

4.1.4 Maximum Deflection

The maximum deflection of the specimens changes greatly based on the curvature of the specimen. The higher the camber of the specimen, the greater the deflection it experiences during impact. Thus, the specimen with higher curvature has a larger camber resulting in a larger maximum deflection.

4.2 Energy Profile

The equations for determining the impact energy are given below in Equation (4.2.1) and Equation (4.2.2). The impact velocity is determined by two factors. The first is the energy due to kinetic energy, which is the first term of Equation (4.2.1). The variable m is the mass of the crosshead/tup. The initial velocity v_i is determined by Equation (4.2.2), which is also the impact velocity measured by the infrared sensor/emitter. The second component of the impact energy is the potential energy generated by the deflection of the specimen during impact. The additional variables of Equation (4.2.1) is g the acceleration of gravity and h' the maximum deflection of the specimen. The maximum deflection is determined by finding the deflection where the extension line intersects the abscissa for open curves. For closed curves, it is the maximum deflection the specimen ever experiences.

$$E_i = \frac{1}{2} m v_i^2 + mgh' = mgh + mgh' \tag{4.2.1}$$

$$v_i = \sqrt{2gh} \tag{4.2.2}$$

The energy profile is the key to characterizing the energy absorption of the composite. The energy profiles shown in Figure 4.2.1 are for a bolted flat panel and bolted medium arch. The impact energy (E_i) is plotted on the abscissa and the absorbed energy (E_a) on the ordinate. The scales for both axes are intentionally the same such that a line can be drawn at a 45° angle, which is the equal energy line. Any data point that lies on this line means for that given impact energy the specimen absorbed all of that energy. At the upper end of the energy profile, the absorbed energy is very close to the impact energy. Once perforation or complete breakdown of the specimen is reached, the specimen has

absorbed the maximum amount of energy. As a result, the data points move away from the equal energy line for increasing impact energies. In this particular case, the perforation energy or the maximum absorbed energy is 91J for the medium arched specimen and 50J for the flat panel.

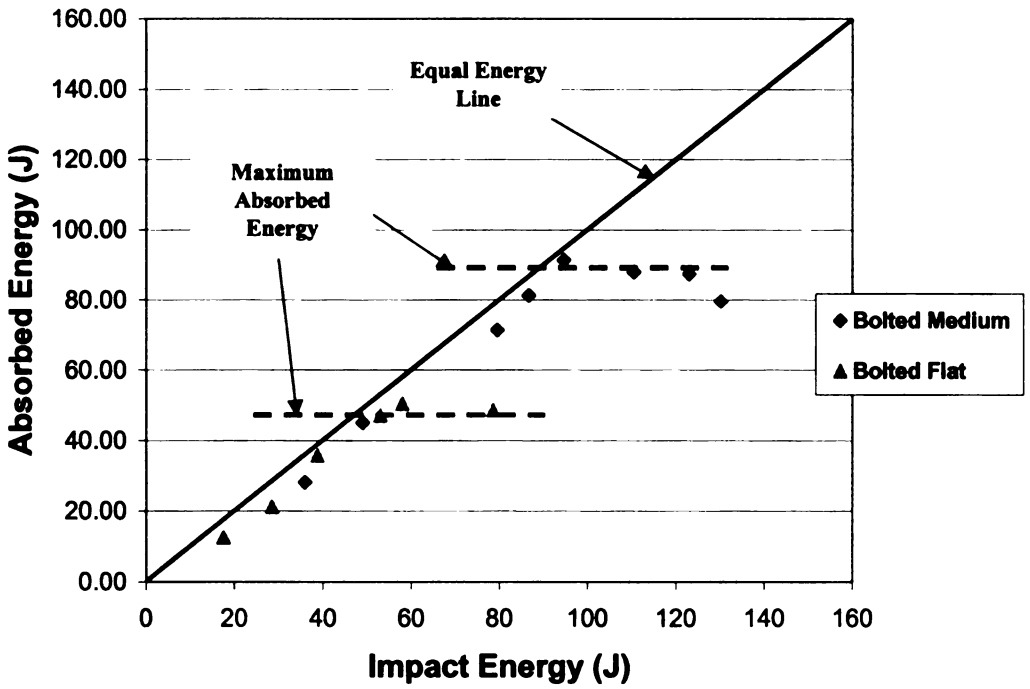

Figure 4.2.1 Energy profiles for bolted flat panel and bolted medium arch specimens.

5. FLAT PANEL BOUNDARY CONDITION STUDY

Studying the effects of the boundary conditions on a conventional flat panel gives insight into the effects the boundary has on energy absorption. A composite beam is fixed on two sides, but a composite plate on four. For the $[0/90]_{3s}$ composite beams the fibers in the transverse direction (90°-plies) do not contributed to the impact resistance as much as those in the axial direction, i.e. the 0°-plies. However, the fibers in both the 0°-plies and 90°-plies contribute to the impact resistance in the $[0/90]_{3s}$ composite plates. Correlating the results from these two studies provides some insight into how the energy is absorbed.

5.1 Boundary conditions and specimens

The boundary effects study of a plate versus a beam for flat panels with $[0/90]_{3s}$ stacking sequence are given below. The beam problem has the same frame clamped boundary condition as the arched composites. The plate problem is frame clamped on all four sides instead of the two ends for the beam problem. Figure 5.1.1 shows schematics of the specimen geometry with the hatched regions showing the clamped areas. The first diagram, Figure 5.6.1(a), is a 102mmx102mm (4"x4") plate with 12.7mm (0.5") clamped on all four sides. Figure 5.6.1(b) is the beam with dimension of 127mmx76.2mm (5"x3") where 25.4mm (1") on either end are clamped.

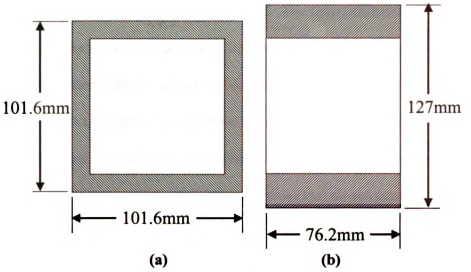

Figure 5.1.1 Flat panels (a) plate (b) beam.

5.2 Load-deflection curves for beam and plate

The load-deflection curves for the two structures, i.e. beam and plate, can be seen below. Figure 5.2.1 is the load-deflection curves for the plate with the four frame clamped edges. The average peak load is 6947N. The maximum deflection is 11.9mm

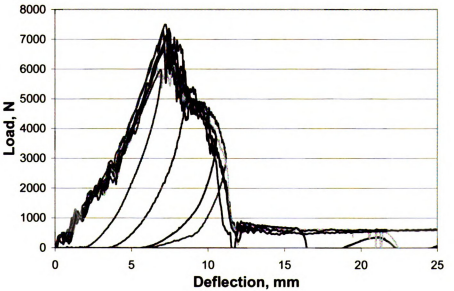

Figure 5.2.1 Load-deflection curves for flat plate with four frame clamped edges.

for the open curves where perforation is achieved. The initial stiffness of the structure is 813 N/mm while the second stiffness is 1,333N/mm.

The load-deflection curves for the beam are given in Figure 5.2.2. The average peak load is 6161N. The maximum deflection for the open curves ranges from 15.6mm to 20.9mm. Notice that two of the closed curves have maximum deflection greater than the three open curves. The maximum deflections of these two closed curves are 20.9mm to 23.6mm. The explanation for the large deflections without perforation is that slippage occurred in the clamping system in the beam problem. The beam stiffness is 62 N/mm for the initial stage and for the second stage 584N/mm. The lower stiffness in the second stage is due to the fibers in the transverse direction not being utilized.

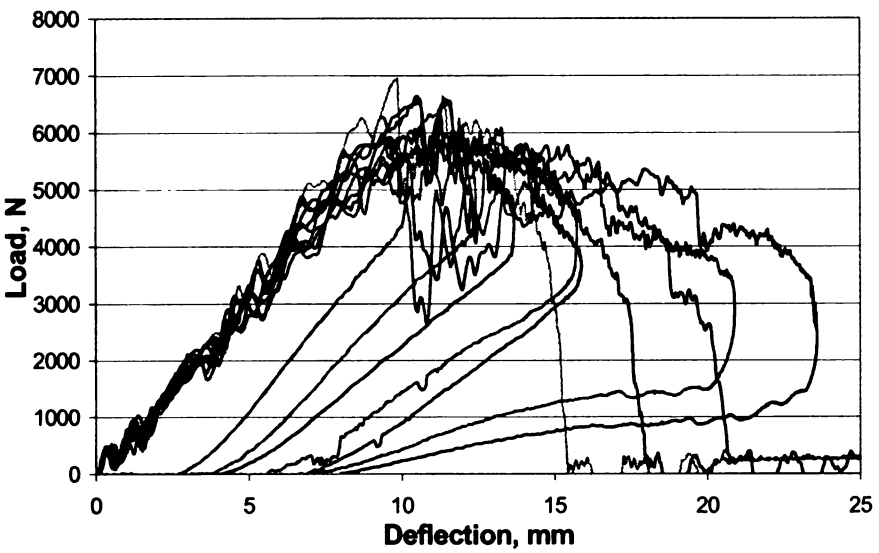

Figure 5.2.2 Load-deflection curves for flat beam with two ends frame clamped.

5.3 Energy profile

The energy profiles for both the beam and plate are given in Figure 5.3.1. The diamonds are for the plate data points and the squares are for the beam. The plate has a clear maximum absorbed energy at 40J of energy. The beam on the other hand continues

to absorb energy, even at 83J. The beam does not absorb all of the impact energy even for low impact energies, but the plate performs slightly better for the impact energies below 40J.

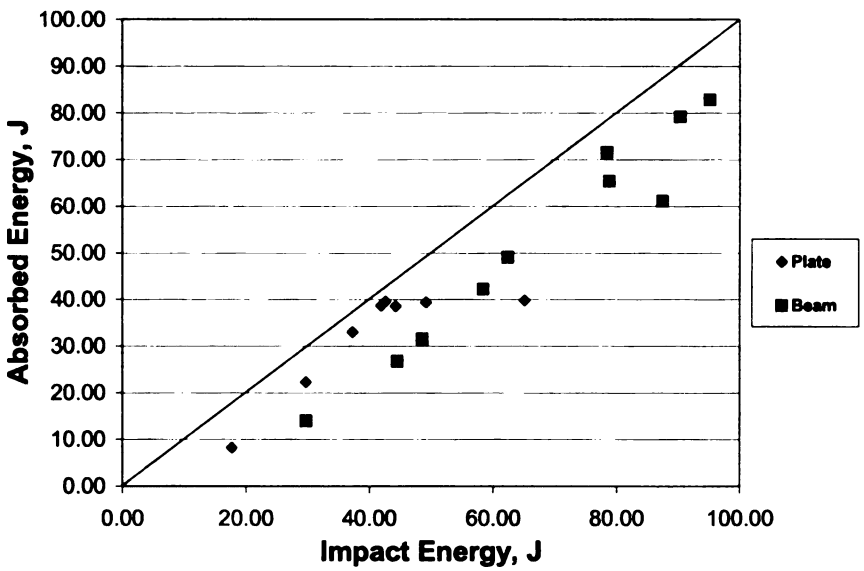

Figure 5.3.1 Energy profiles for both plate and beam.

5.4 Characteristics of impact response

The impact characteristics give a picture of the behavior of each boundary condition and their contribution to energy absorption. The characteristics are stiffness, peak load, deflection at the peak load, maximum deflection, and absorbed energy. Table 5.4.1 contains the averages for each characteristic in bold with its standard deviation next to it.

The plate has the higher stiffness of 834N/mm and 1,333N/mm in both the initial and second stiffness. The plate also has the higher peak load. Taking into account the standard deviation for the peak load, there is a difference. For the plate, there are two

Table 5.4.1 Impact characteristics for plate and beam.

	Stiffness 1 (N/mm)	Stiffness 2 (N/mm)	Peak Load (N)	Deflection @ peak load (mm)	Max Deflection (mm)	Absorbed Energy (J)
Plate	**834**/108	**1333**/116	**6947**/548	**7.3**/0.27	**11.9**/0.19	**40**
Beam	**620**/44	**584**/75	**6161**/472	**10.8**/1.52	**18.1**/2.70	**83**

results that push the standard deviation from 159N to its current 548N. It is also clear that the deflection at the peak load is lower for the plate than for the beam.

Since the plate is fixed on four sides, it is stiffer and produces a larger peak load with a smaller deflection. Because of the plate's high stiffness and small deflection, it produces load-deflection curves that are triangular like shape, which have less area under them. The larger loads will produce fiber breakage for the same plate that would not cause fiber breakage in the beam.

5.5 Summary

In terms of energy absorption, the beam clearly absorbs more energy without breaking. The trade off is that lower stiffness and larger deflection. The beam is 25.6% less stiff than the plate, but absorbs nearly 50% more energy without as much damage. The deflection is the main contribution of the energy absorption because the maximum deflection is almost twice in the beam for the doubling of energy absorption. This is only the case because the peak load is slightly lower in the beam case. It is likely that the friction forces around the clamped boundaries decrease deflection of the specimen, but increase the peak loads. The clamping boundary forces are critical to prevent slippage, which would allow for increase energy absorption. But the beams can deflect more than the plate due to the free boundary on the two sides.

6. BOUNDARY CONDITIONS AND EFFECTS

The arched composite specimens investigated in this study were of rectangular shape from the top view. Along the longitudinal direction, there was a designated curvature in the middle section and flat wings at the end sections. For impact tests, the composite specimens were clamped to the base plate of the specimen holder of the impact tester by steel bars at the end wings. The specimens were found to pull out of the bars significantly when the impact energy was high, resulting in significant energy absorption due to the friction between the composite specimens and the specimen holder rather than purely due to the damage of the composite specimens.

In order to reduce the friction-induced energy absorption, the composite specimens were clamped by a square frame at the end wings. The frame functioned similarly to the bars except that the two clamping end members were not free to move with respect to each other due to the constraint from two side members. Composite specimens clamped by the frame still showed pullout up to some extent. In order to completely eliminate the pullout phenomenon, four holes, two at each clamping end member, were introduced to the square frame. The composite specimens were then bolted in between the frame and the base plate of the specimen holder before being clamped.

The three methods of holding the composite specimens were titled bar clamped, frame clamped, and bolted boundary conditions. This chapter gave insight into the effects of these boundary conditions on the performance of the arched composites. It covered the load-deflection curve, energy profile, characteristics of impact response and the damage process of individual composites. A thorough understanding of the boundary effects may lead to more effective armor designs.

6.1 Types of Boundary Conditions

There are three clamping boundary conditions in these experiments. Figure 6.1.1 shows all three boundary conditions. Each specimen sits on a frame with a 76.2mmx76.2mm (3"x3") opening and the winged portions rest on either side of the opening. Toggle clamps are used to secure the specimen, where the locations of the feet are given in the diagrams.

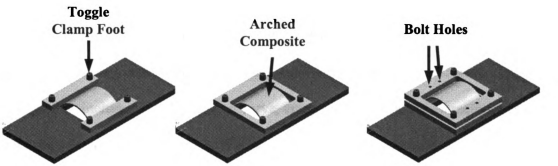

Figure 6.1.1 Boundary conditions types:(a) bar clamped, (b) frame clamped and (c) bolted.

The bar clamped design can be seen in Figure 6.1.1(a). The arched composite sits on the base plate of the specimen holding fixture of the impact tester. Two steel bars 25.4mm (1.0") wide by 12.7mm (0.5") thick clamp the arched composite at the two wings with four toggle clamps. The force of the toggle clamps provides the clamping force that secures the specimen.

Figure 6.1.1(b) shows the frame clamped design. It is very similar to the bar clamped design. The only difference is that the two end members are secured to each other by the two side members, preventing a relative motion between them from occurring. The pullout can take place when the arched composite collapses during impact.

To completely secure the composite to the base plate, the composite is bolted and clamped between two frames. The diagram of this setup can be seen in Figure 6.1.1(c). Two 6.35mm (0.25") bolts are used to secure each wing of the arch composite. With this third boundary condition, the effects of the friction forces between the specimen and the specimen holder are eliminated, allowing analysis of the energy absorption based on the composite damage.

6.2 $[0/90]_{3s}$ Composite with Small Arch Curvature

To analyze the effects of the boundary conditions on the impact response of arched composites, $[0/90]_{3s}$ composite with a small curvature was investigated. The investigations included load-deflection curve, energy profile, impact characteristics and the damage process. The results could give insight to the energy absorption of the arch composite. The small arch has a radius of curvature of 84.14mm (3.31") and a camber of 7.95mm (0.313").

6.2.1 Load-deflection Curves

Figure 6.2.1 shows the load-deflection curves for the small arched composites with the bar clamped boundary condition. There is a sharp rise in load with the peak between 3,000N and 4,000N at a deflection ranging from 8.2mm to 9.6mm. The load decreases significantly, and then remains relatively constant before decreasing to failure gradually. Failure is difficult to define because the specimen slips in the clamps. The maximum deflection is on average 55mm.

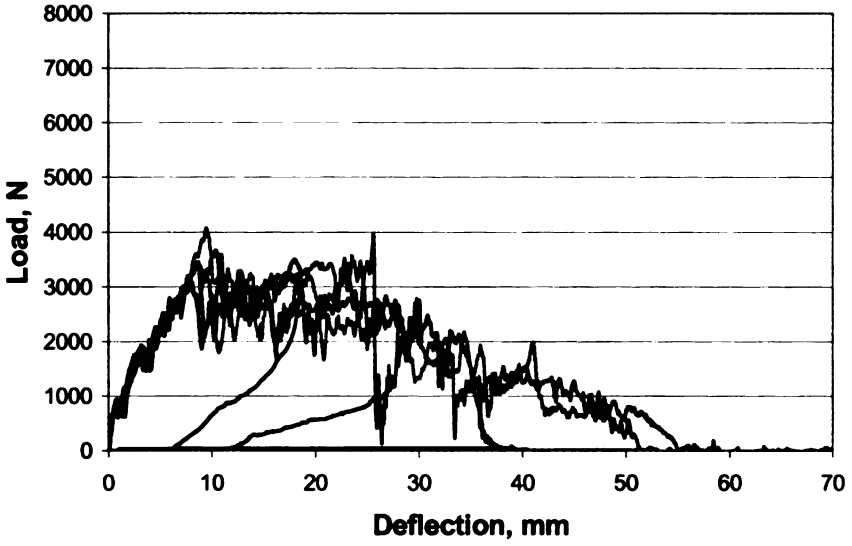

Figure 6.2.1 Bar clamped $[0/90]_{3s}$ with small arch.

For the frame clamped boundary condition, the load-deflection curves can be seen in Figure 6.2.2. Once again, there is a sharp rise in load before it levels off with large oscillations. Because of the oscillations, it is difficult to define the peak load without averaging out the oscillations. The maximum loads right after the initial rise ranges from 2,000N to 4,300N at a deflection of 13.6mm. The maximum deflection is at 60mm, but

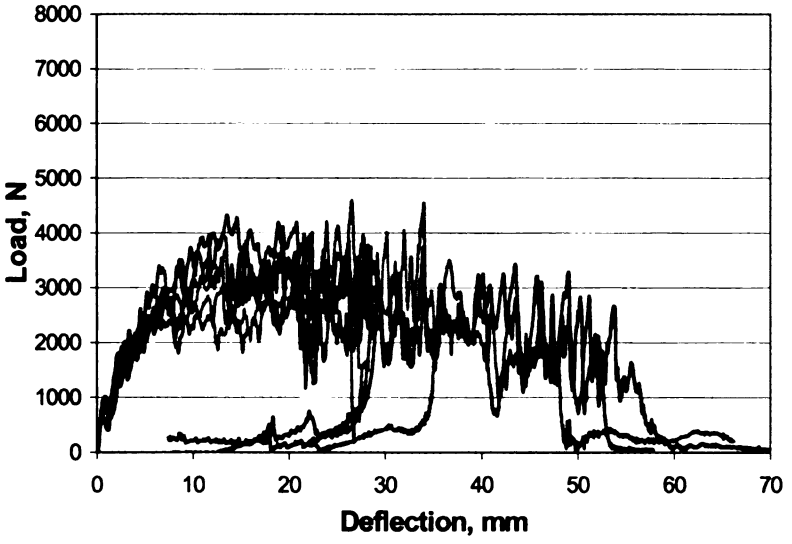

Figure 6.2.2 Frame clamped $[0/90]_{3s}$ with small arch.

failure also occurs at 48mm and 54mm of deflection.

For the third boundary condition where the specimens are bolted in place, the load-deflection curves are shown in Figure 6.2.3. Again, there is a sharp rise in load, then decreases sharply. Once the local minimum is reached the load again increases to a peak range from 5,990N to 6,760N at deflections 21mm to 23mm. The deflection at failure ranges from 29mm to 34mm.

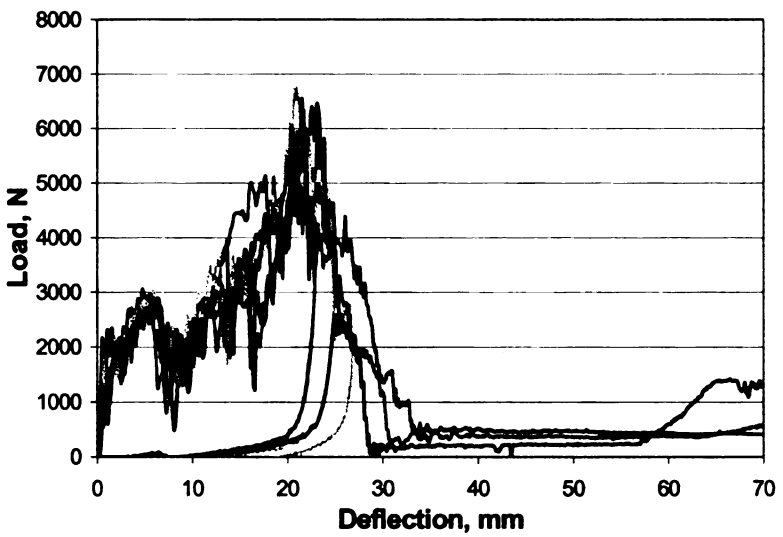

Figure 6.2.3 Bolted $[0/90]_{3s}$ with small arch.

As the boundary conditions become more constrained, the results become more consistent. Because of the large forces generated during impact, bolting the specimen in place was the only guaranteed way to assure a fixed boundary condition. The slippage decreased the peak load from approximately 7,000N to 4,000N while increasing the maximum displacement from 34mm to 60mm. The load-deflection curves changed from a flat plateau for the clamped design to a double-peak mountain shape.

To make a comparison among the load-deflection curves from all three types of boundary conditions, they are plotted on the same graph. Figure 6.2.4 shows a typical

curve representing each type of boundary condition for the $[0/90]_{3s}$ composite with a small arch. Notice how the bolted design reaches the first peak load at about 6mm of deflection, but the other two boundary conditions allow the load to peak at a larger load at 10-15mm. The bolted however peaks at 6000N at about 22mm, whereas the other two boundary conditions have had a decrease in load to an approximate average of 2,500N. The bolted design fails at a much lower deflection. The bar clamped does decrease the load at a faster rate than the frame clamped.

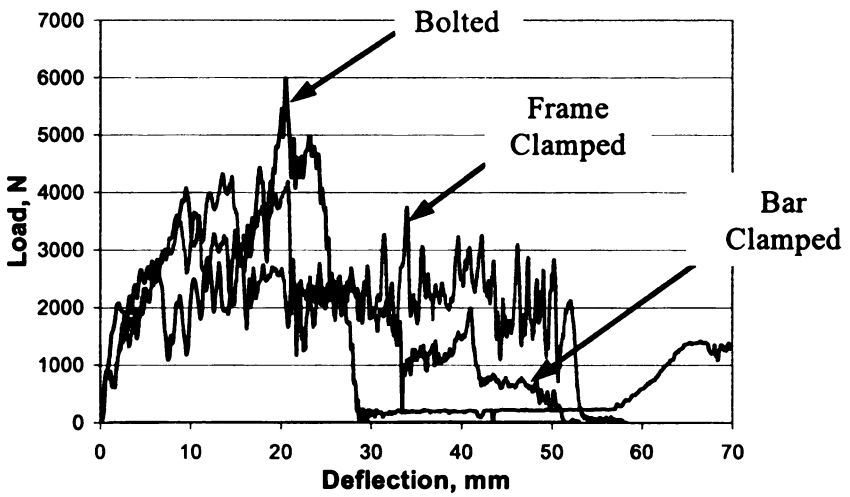

Figure 6.2.4 Typical load-deflection curves from the three types of boundary conditions for $[0/90]_{3s}$ with small arch.

From a design perspective, a semi-fixed boundary condition may be ideal as the objective is to increase the area under the curves. Purely fixed, such as bolted, increases the load but limits the deflection of the specimen whereas too much slippage allows just the opposite. Therefore, a semi-fixed clamping system would potentially provide the most desirable load-deflection curves. An energy analysis may help to verify the claim.

6.2.2 Energy Profile

Figure 6.2.5 shows the energy profiles for the load-deflection curves from Figures 6.2.2, 6.2.3, and 6.2.4. The diamond data points are from the bar clamped, the squares are from the frame clamped and lastly the triangles are from the bolted design. The plot shows that the impact energy approaches the absorbed energy as it increases, i.e. the impact is almost completely absorbed by the composite in each case. For both the bar and frame clamped, however, it is difficult to distinguish a perforation point. This is due to the specimen being pulled out of the clamping system, instead of being damaged by perforation. At E_a=82J the bolted specimens has the closest value between the impact and absorbed energy implying the penetration energy point is near. The bar clamped has a higher maximum absorbed energy around 95 Joules due likely to the slippery boundary condition. The frame clamped is absorbing nearly all 140J of impact energy from the highest impact energy test conducted. The reason for this performance could be that the clamping was improved, but it was not so firm that slippage could be avoided. It is

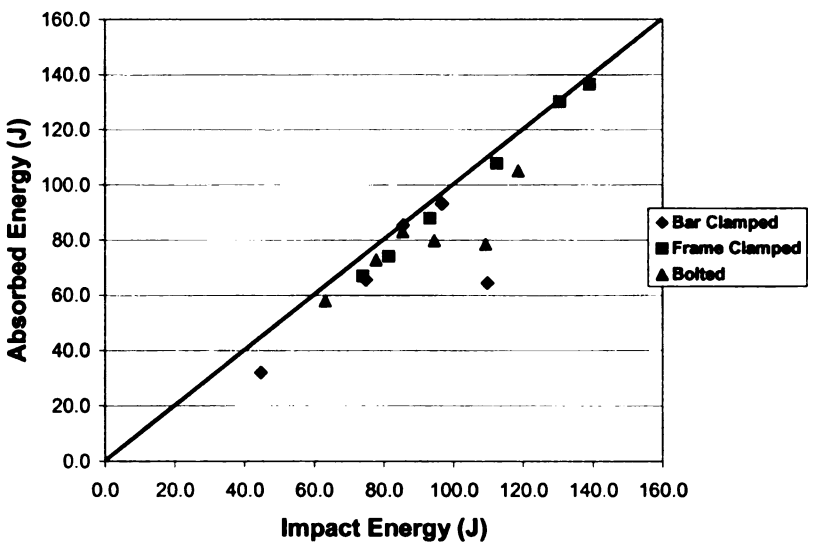

Figure 6.2.5 Energy profiles for $[0/90]_{3s}$ with small arch for all three types of boundary conditions.

believed that the slippage and larger associated deflection of the specimen are what allowed this higher energy absorption. Besides, it should be pointed out that regardless of the type of boundary condition, the maximum absorbed energies of the arched composites are much higher than that of flat counterpart, implying that an arch is an efficient design to improve the energy absorption capability. Moreover, with an adequate slippage in the boundary, the highest maximum absorbed energy can be further increased.

6.2.3 Characteristics of Impact Response

The characteristics of the impact response of composites are the stiffness, the peak load, the maximum deflection, contact duration, and energy absorption. Table 6.2.1 shows averaged results for the three boundary conditions for the composites with small arch. The slope of the initial rise in the load is the stiffness. The frame clamped has a slightly lower stiffness than the bar clamped. The bolted specimen a stiffness that is middle of the range, where there is overlap in the results.

Table 6.2.1 Characteristics of impact response for $[0/90]_{3s}$ with small arch.

Boundary Condition	Stiffness (N/mm)	Peak Load (N)	Deflection @ peak load (mm)	Max Deflection (mm)	Contact Duration (ms)	Absorbed Energy (J)
Bar	285	3802	15.9	49.0	33.2	93
Frame	262	4119	18.4	54.3	28.5	136.4
Bolt	276	6294	21.9	31.3	10.8	83.0

The bolted design has the largest peak load, 6,294N, which was after the first peak load. The deflection at the peak load for the bolted design occurred at 21.9mm of deflection. The frame clamped has the peak force right after the initial rise in loading except one curve with large oscillations causing the peak load late in the damage process

(see Figure 6.2.2). The peak load of the bar clamped is slightly smaller than that of the frame clamped.

The frame clamped has the largest maximum deflection at 54.3mm, which is 9.8% larger than the bar clamped at 49mm. The bolted specimens had a maximum deflection of 31.3mm. This matches with the fact that they were not allowed to deflect as much due to the bolting.

The contact durations for the bar and the frame clamped boundary conditions are very similar. The bolted design has a much lower contact duration around 10.8ms. The result from the contact duration seems to match with that from the maximum deflection.

The energy absorption is the perforation or maximum absorbed energy by the specimens. The frame clamped absorbs the most energy at 136.4J with the bolted absorbing the least at 83.0J. It is evident that the clamping boundary conditions absorb energy.

6.2.4 The Damage Process

The damage process for the arched composite was much different than flat panels. The arched specimens went through a large deflection process due to buckling and bending. The arches had much greater delamination and ended in an inverted state when damaged. The composite was damaged by initial indentation, fiber breakage, and delamination. If the specimen is bolted, it will buckle, causing the initial peak and load drop in the load-deflection curves. The bar and frame clamped load-deflection curves are much different in that there are not noticeable peaks. The slippage at the boundary condition reduced the buckling effects causing the change in the load-deflection relation.

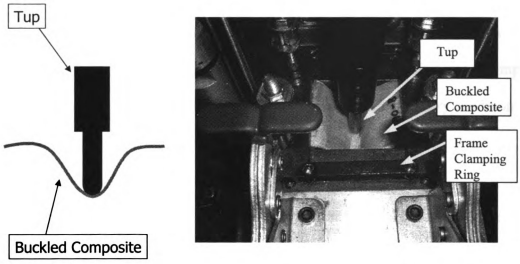

(a) **(b)**

Figure 6.2.6 (a)Schematic diagram of tup and buckled arch composite and (b)photograph of schematic in (a).

The arched composites went through a stage when the sides bend until the composite was in an inverted state. Figure 6.2.6 shows the tup and inverted composite interaction. Figure 6.2.6(a) is a schematic and Figure 6.2.6(b) is an actual top view of their interaction. Notice how the tup rubs against the composite and is slightly wedged. This frictional interact can be another mode of energy absorption.

When perforation happened, sometimes the tip left a hole at the center of the specimen and other times there were enough delamination, matrix cracking and fiber breakage across the width of the specimen to cause the composite to break into two pieces. More commonly, the specimen would pull out of the clamps before being perforated. The bolted design eliminated the pullout and increased the amount of damage in the specimen.

The boundary condition affects the damage process and the energy absorption of composite. The damage process is similar for all boundary conditions up to some extent.

Once enough force is transferred to the boundary, the bar clamped or the frame clamped composite can slip. When a composite slips, instead of being damaged, some of its structural integrity is maintained. On the contrary, the bolted design increases the impact load and decreases the deflection of the composite. A semi-fixed boundary condition allows larger slippage, reducing the buckling effects.

6.3 $[0/90]_{3s}$ Composite with Medium Arch Curvature

To present all of the data in regards to the effects of the boundary conditions, the results from the composites with medium arch are given in this section. The medium arch has a larger camber and curvature than the small arch. The medium arch has a radius of curvature of 57.15mm (2.25") and a camber of 15.88mm (0.625"). That is, the radius of curvature for the medium arch is smaller than that for small arch. The curvature effects will be mentioned in chapter 7.

6.3.1 Load-deflection Curves

Figure 6.3.1 shows the load-deflection curves for the bar clamped boundary condition

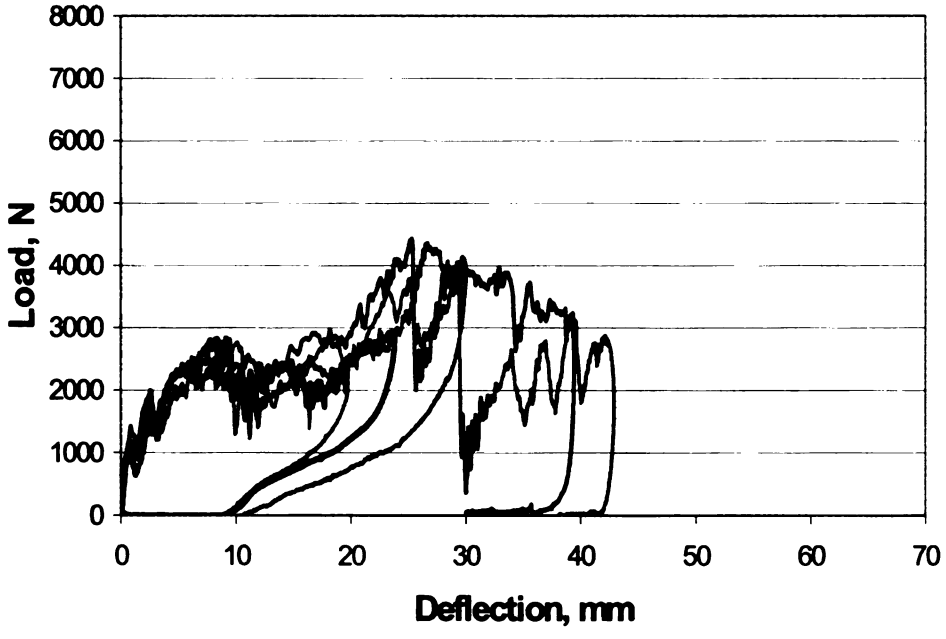

Figure 6.3.1 Bar clamped $[0/90]_{3s}$ with medium arch.

of the medium arched composites with a stacking sequence of $[0/90]_{3s}$. The peak loads range from 4423N to 3936N at deflections of 25.3mm and 29.4mm, respectively. The maximum deflections range from 39.4mm to 42.9mm. Notice that the load has an initial maximum about 8.6mm of deflection, then drops off and finally increases to the peak loads before reducing.

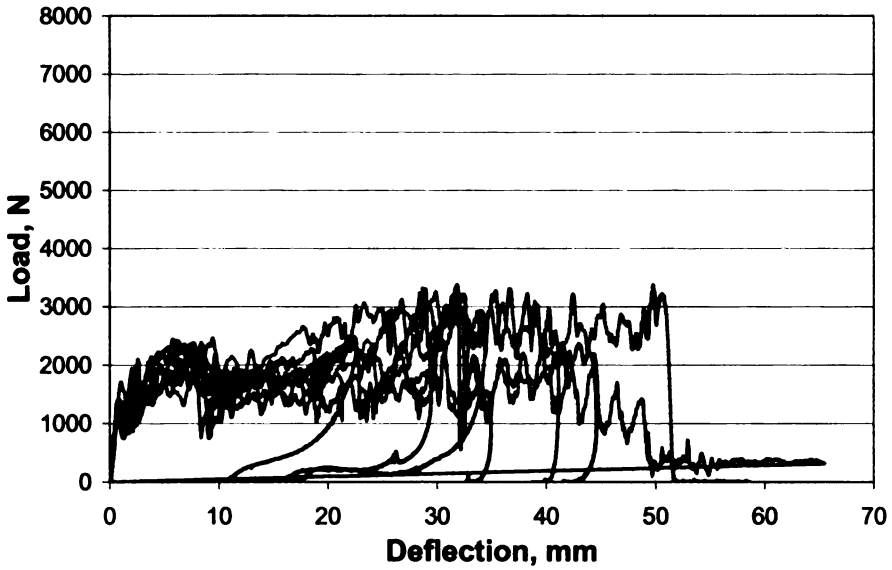

Figure 6.3.2 Frame clamped $[0/90]_{3s}$ with medium arch.

The results for the frame clamped boundary condition can be seen in Figure 6.3.2. The peak load ranges from 2382N to 3376N and the deflection at the peak load ranges from 9.4mm to 49.8mm. The maximum deflections range from 34.9mm to 51.7mm. It can be seen from the diagram that this boundary condition has a saddle-like region, but the peak load is maintained for a deflection of approximately 20mm.

The load-deflection results for the bolted specimens can be seen in Figure 6.3.3. In comparison to the small arch, the load-deflection curves look very similar. There is the initial increase in load, then a sharp decline followed by another increase to the peak load. The peak load ranges from 5123N to 6869N and the deflections at the peak load

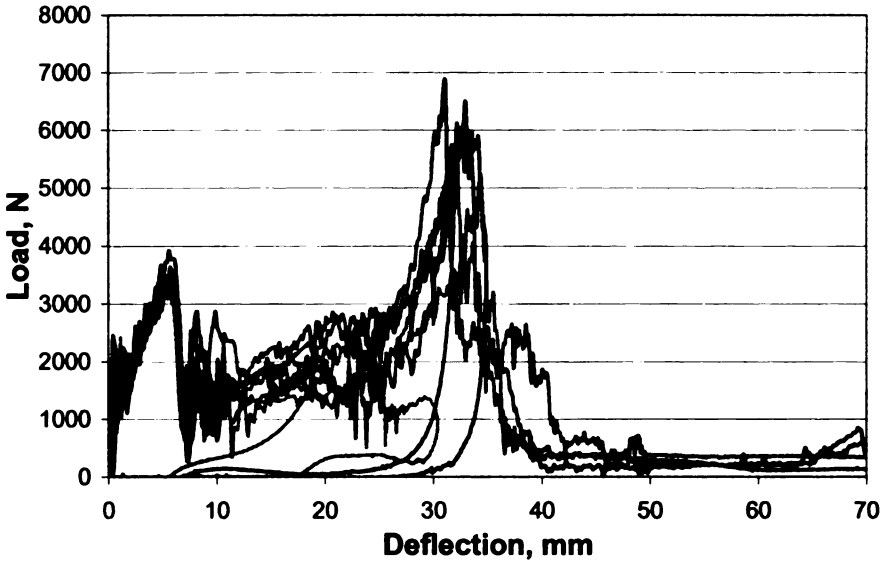

Figure 6.3.3 Bolted $[0/90]_{3s}$ with medium arch.

ranges from 31.1mm to 34.3mm. The maximum deflection reaches a range from 41mm to 46.5mm.

6.3.2 Energy Profile

The energy results from the calculated impact and absorbed energies can be seen in

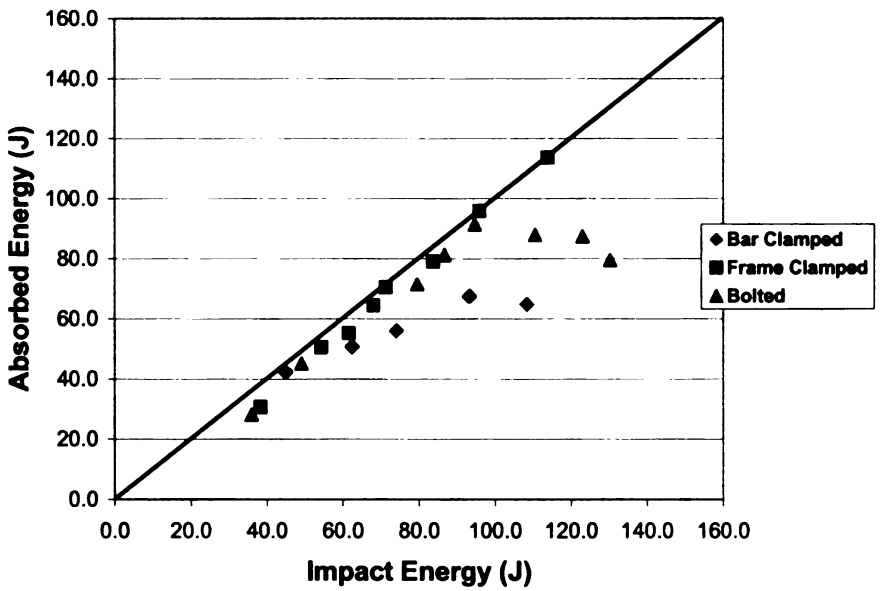

Figure 6.3.4 Energy profiles for medium arch curvature $[0/90]_{3s}$ for all three boundary condition types.

Figure 6.3.4, where all three boundary conditions are included. The diamonds are for the bar clamped, the squares for the frame clamped, and the triangles for the bolted. The data points located on the diagonal line mean that the specimens absorb all of the impact energy. Beyond E_i=70 Joules, the specimens can no longer absorb the energy efficiently. The frame clamped shows nearly complete energy absorption at all impact energies up to 114 Joules, which is the highest impact energy performed. For the bolted boundary condition the most energy the specimen can absorb is 91 Joules.

Similar to the small arched composites, the medium arched composites absorbed the highest energy among the three types of boundary conditions, due likely to the most effectiveness of the frame clamped boundary condition. They could absorb much of the energy at lower impact energies and almost all energy at higher impact energies. The clamping force seemed to be around an ideal level.

6.3.3 Characteristics of Impact Response

Characteristics of the impact response of the composites with medium arch are summarized in Table 6.3.1 where all of the results are based on average. The stiffness is lowest for the frame clamped and more than doubles for the bolted specimens. The peak load is also much greater for the bolted specimens. However, being different from that of small arch, the peak force for the frame clamped is smaller than that for the bar clamped in the medium arched composites. Another difference occurs in the maximum

Table 6.3.1 Characteristics of impact response for $[0/90]_{3s}$ medium arch.

Boundary Condition	Stiffness (N/mm)	Peak Load (N)	Deflection @ peak load (mm)	Max Deflection (mm)	Contact Duration (ms)	Absorbed Energy (J)
Bar	427	4236	27.1	41.1	19.6	67.4
Frame	236	2884	30.8	44.4	29.1	113.6
Bolt	576	5984	32.4	40.6	13.5	91.3

deflections. They are very close for all boundary conditions. However, it should be pointed out that both the bar clamped and the frame clamped specimens tested did not reach the maximum capacity of the composites as can be seen in Figures 6.3.1 and 6.3.2, i.e. the load-deflection curves do not decrease to zero gradually as those shown in Figures 6.2.1 and 6.2.2 for small arched composites. Although the maximum deflections are similar among the different boundary conditions, the contact durations for open curves are not. The shortest contact duration is the bolted specimen at 13.5ms and the frame clamped with the longest contact duration at 29.1ms.

6.3.4 The Damage Process

The damage process for the medium arch follows similar process to the small arch. The largest difference is that the medium arch has to travel more distance before the arch collapses. This distance can be seen in Figure 6.3.2 where the transition from the first peak load to the second peak load is longer for the bolted specimens. The bar and frame clamped boundary conditions allow slippage of the specimen so there is not definite second peak load when the arch inverts as seen in Figures 6.3.1 and 6.3.2.

6.4 $[0/90]_{3s}$ Composite with Large Arch Curvature

The results for the large arch composites are given in this section. The radius of curvature is 44.45mm (1.75") with a camber of 20.65mm (0.813") at the peak. Because this design has the smallest radius of curvature, the sides of the arch are more vertical than the other two designs and the camber is the greatest.

6.4.1 Load-deflection Curves

The load-deflection curves for the bar clamped boundary condition are shown in Figure 6.4.1. The peak load ranges from 237N to 3754N at deflections 6.6mm and

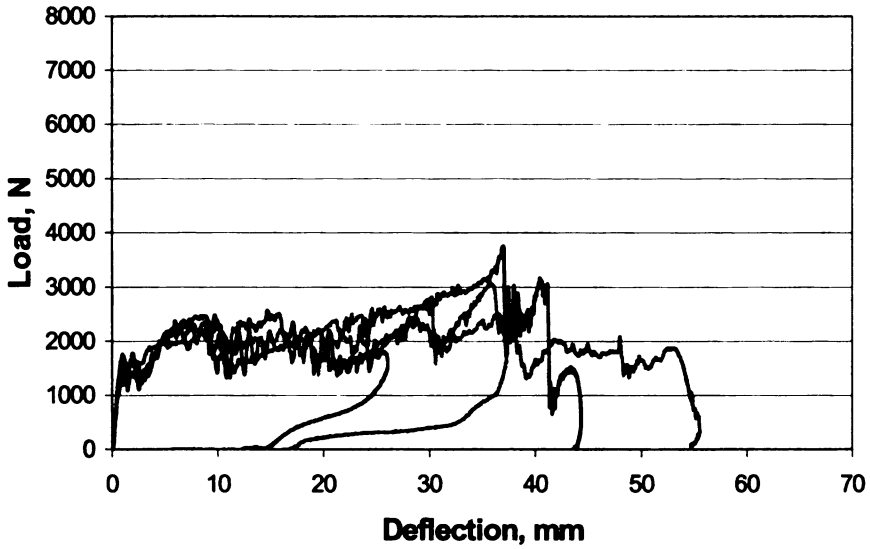

Figure 6.4.1 Bar clamped $[0/90]_{3s}$ with large arch.

37.0mm, respectively. The maximum deflections are at 44.0mm and 55.6mm. It can be seen that the peak loads seem to occur in the later part of the curves.

Figure 6.4.2 shows the load-deflection curves for the frame clamped boundary condition for the large arch. The peak load ranges from 2815N to 4649N with their deflections ranging from 34.0mm to 43.4mm. The maximum deflections for the two final curves are 59.8mm and 69.2mm. In this case the larger deflection is due to higher impact

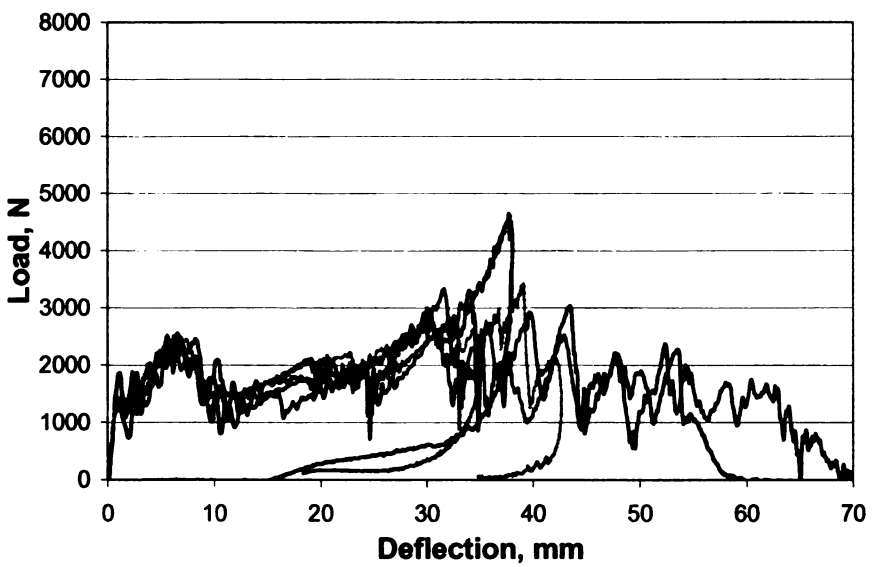

Figure 6.4.2 Frame clamped $[0/90]_{3s}$ with large arch.

energies promoting slippage of the specimen. The larger the impact energy, the more the specimen pulls out of the clamping system, which allows it to deflect more. Hence, care should be exercised in the comparison of energy absorption capability.

The results for the bolted specimens are shown below in Figure 6.4.3. The general trend of these load-deflection curves is similar to the results from the small and medium arches. The major difference, however, is the large saddle after the first peak. The average load in this saddle region is about 1,500-2,000N and increases to the second peak at about 30mm of deflection. The second peak load ranges from 3,374N to 6,470N with a corresponding deflection ranging from 50.0mm to 61.9mm. The second peak loads are actually slightly lower than the initial peak load for some cases. Also, there is some variation in the location of the peak load.

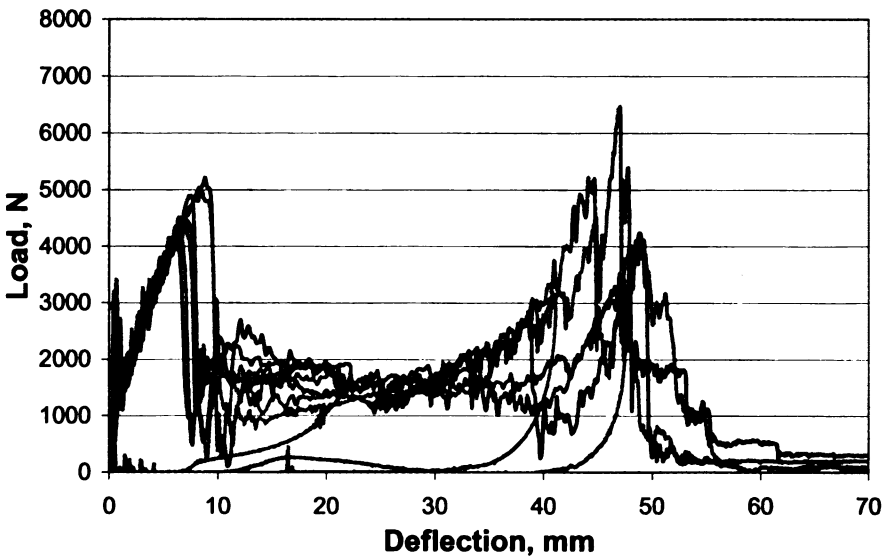

Figure 6.4.3 Bolted $[0/90]_{3s}$ with large arch.

6.4.2 Energy Profile

The energy profiles for all three boundary conditions for the large arch can be seen in Figure 6.4.4. The diamond data points are for the bar clamped specimens, the squares for

the frame clamped, and the triangles for the bolted. The bar clamped data points appear to have a "perforation" point at 100 Joules. The frame clamped specimens appear to absorb most of the impact energy up to 113 Joules. The bolted specimens absorb a maximum energy of 107 Joules. All three designs seem to absorb about the same amount of energy for the impact energies tested.

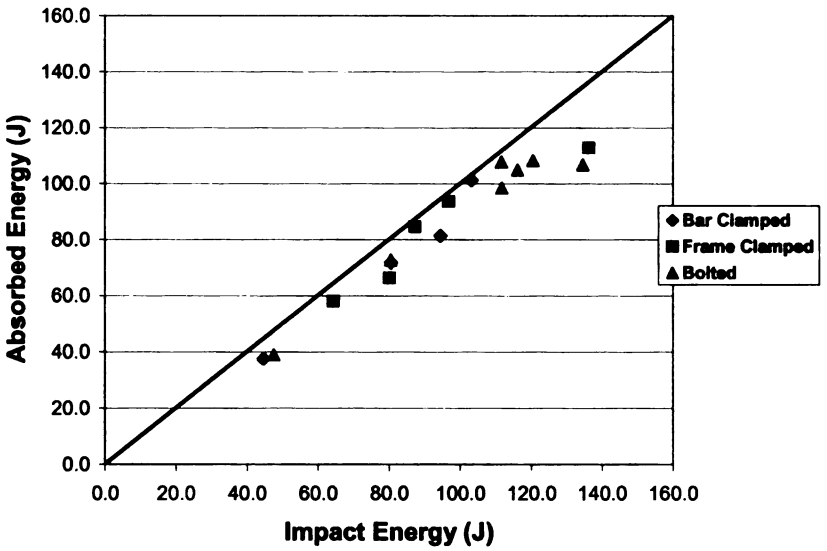

Figure 6.4.4 Energy profile for $[0/90]_{3s}$ with large arch for all boundary conditions.

6.4.3 Characteristics of Impact Response

The characteristics of the impact response for the large arch specimens are summarized in Table 6.4.1, where all the values are averages. Again the stiffness is much larger for the bolted specimens than for the bar or frame clamped because slippage cannot occur in the bolted specimen. The peak load for the bolted specimens is the largest, with the bar clamped having the smallest peak load. The frame clamped however, had the largest maximum deflection. The bolted specimens have the lowest contact duration with the bar clamped specimens with the largest contact time. The result

of the contact duration is not consistent with the result of the maximum deflection as that occurs in the small arch specimens.

Table 6.4.2 Characteristics of impact response for $[0/90]_{3s}$ with large arch.

Boundary Condition	Stiffness (N/mm)	Peak Load (N)	Deflection @ peak load (mm)	Max Deflection (mm)	Contact Duration (ms)	Absorbed Energy (J)
Bar	327	2918	29.0	49.9	48.4	101.2
Frame	280	3444	37.2	64.5	30.5	93.5
Bolt	570	4702	47.4	56.6	20.5	107.8

6.4.4 The Damage Process

The damage process for the large arch again is most similar to the medium arch. The major difference is that more deflection must take place to initiate the peak load for the bolted specimens. This deflection will cause more delamination as the sides buckle inwards to the inverted state.

6.5 Summary of results

Each boundary condition produces different results with energy absorption being the primary focus. A composite diagram of the results seen in this chapter are summarized in Figure 6.5.1. The data is organized such that each arch and boundary condition is labels on the x-axis where the abbreviations are: small bar clamped (SBC), small frame clamped (SFC), small bolted (SB), medium bar clamped (MBC), medium frame clamped (MFC), medium bolted (MB), large bar clamped (LBC), large frame clamped (LFC), and large bolted (LB). The stiffness numbers have been divided by 10 and peak loads (PL) by 100 for scaling purposes.

The most noticeable feature is that the bolted specimens have the largest peak load. The small arch has the largest peak load with the large arch with the smallest peak load. The frame clamped boundary condition has the largest maximum deflection for each arch size. This large deflection is one of the contributing factors to energy absorption.

Further details on the curvature effects on energy absorption will be covered in the following chapter.

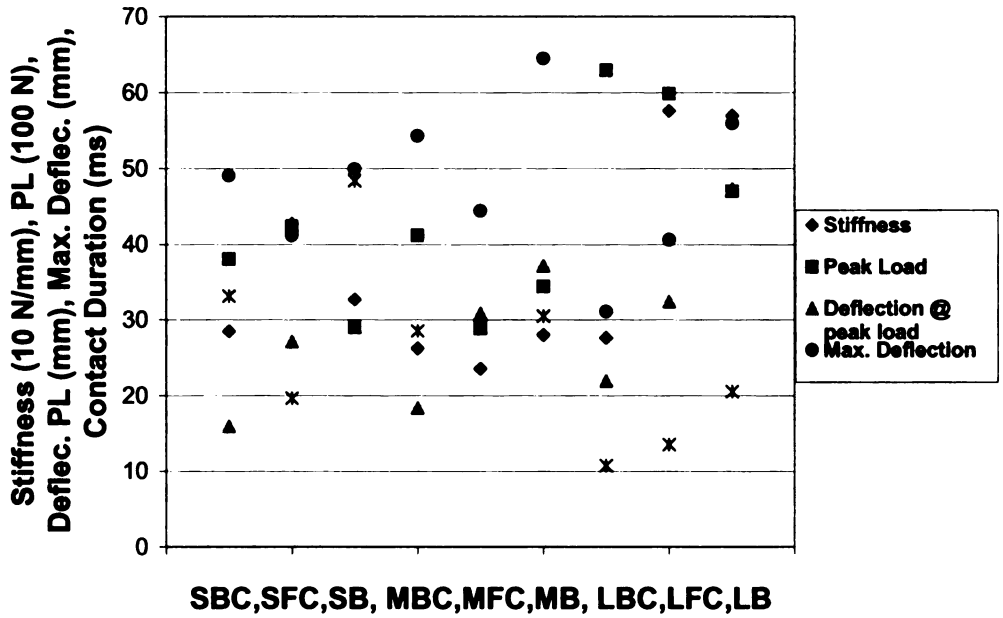

Figure 6.5.1 Composite diagram of impact characteristics.

7. CURVATURE AND EFFECTS

The effects of the arch curvature on the load-deflection relation should provide insight to an even more effective design for energy absorption. An ideal armor is one that stops ballistic projectile or blast wave through absorbing all impact energy. With the increase of curvature, a composite specimen has more material aligned along the impact direction, the impact resistance should be increased accordingly. However, the gross mass of the specimen is also increased. An optimal curvature may be identified.

7.1 Load-deflection Curves

Figure 7.1.1 shows a typical load-deflection curve from each of the three types of arch composites with bolted boundary condition as well as a bolted flat composite (zero arch). The flat panel is 69.85mm (2.75") wide like the arches and is 127mm (5") long so that only 25.4mm (1") on each end is clamped like the arches. Several important features

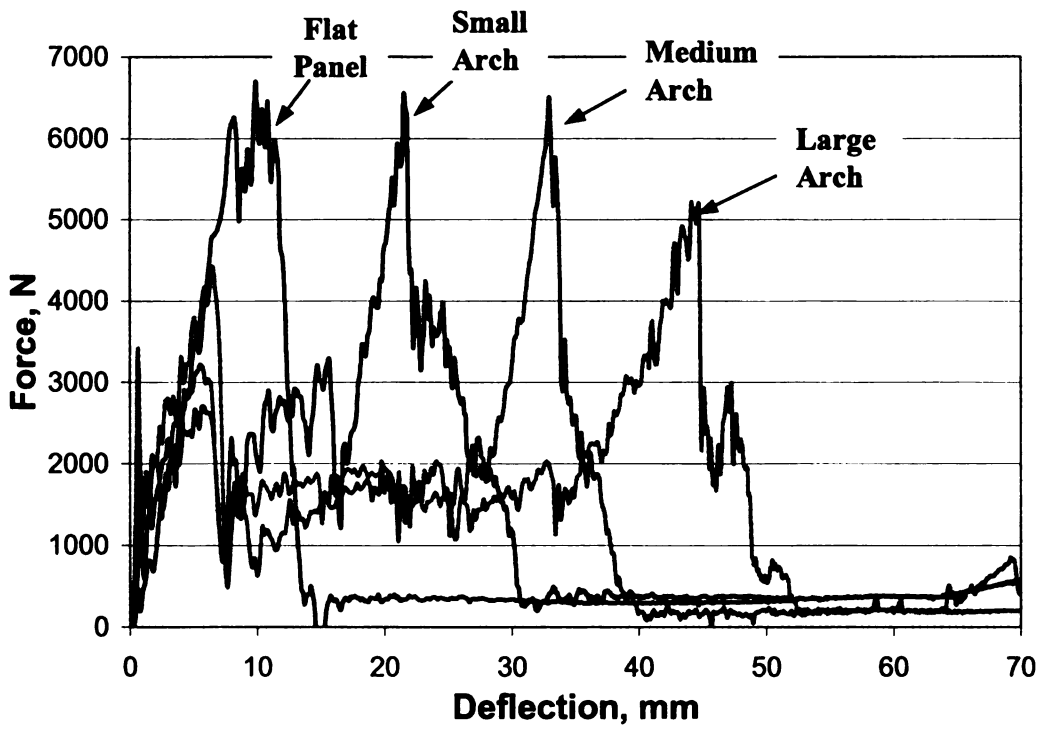

Figure 7.1.1 Typical load-deflection curves for bolted arches and flat panel.

should be noted. There are two main maximum loads

in the arched composites, the first, i.e. the initial maximum load, occurs about 6mm of deflection and the second, i.e. the peak load, is located at different deflection value depending on the arch size. The flat panel has no initial maximum load and its stiffness is similar to those of the arches. For the arch composites, the region between the two maximum loads looks like a saddle shape and tends to increase as the curvature of the composite increases. The flat panel has zero curvature and there is only one peak load and no saddle region.

Measuring the two maximum loads and associated deflections and plotting their relation will help to sort out the curvature effects. Figure 7.1.2 shows a plot for the first peak load and the corresponding deflections for the three arch sizes. The load measurements are taken from individual tests. The diamonds are the data points for the small arches, which have the lowest initial maximum force, followed by the medium arch, and the large arch has the highest initial maximum force. It can be concluded from

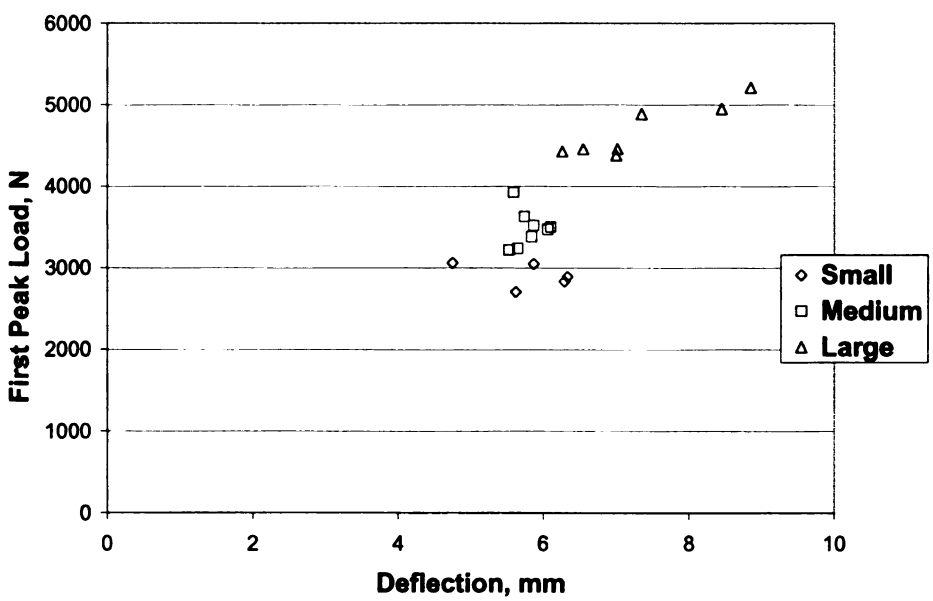

Figure 7.1.2 First maximum load and associated deflection.

this diagram that the initial maximum load increases as the curvature increases. This result is likely due to the fact that more material is aligned along the impact direction when the curvature increases.

The results for the second peak load and corresponding deflections can be seen below in Figure 7.1.3. The general trend is that the peak load decreases as the curvature increases, while the corresponding deflection increases. The increase in the deflection is due to the height of the arch, which allows the composite to deflect more before being perforated. The decrease in the peak load may be due to the fibers not being as stiff because they are not pulled as taunt as a flat panel or small arch.

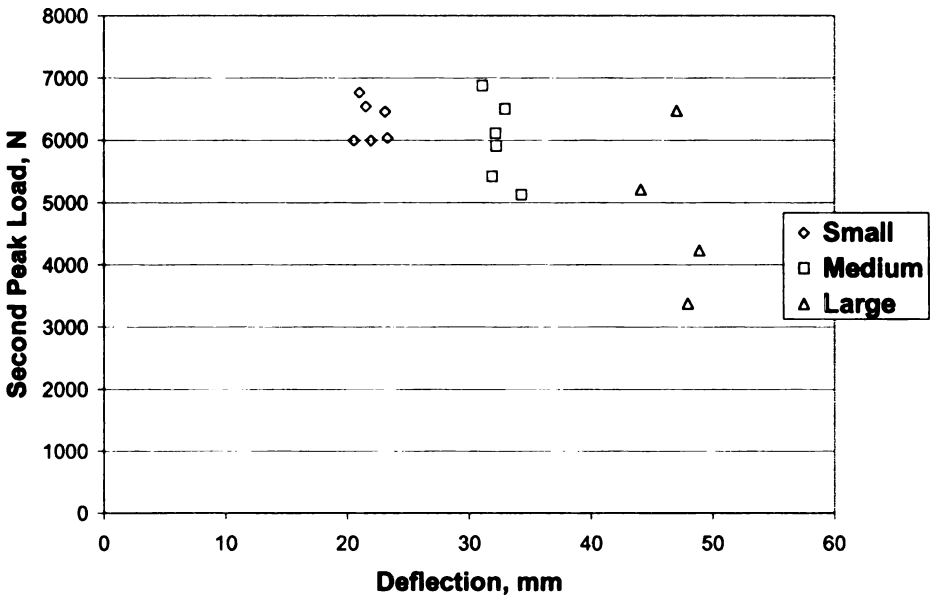

Figure 7.1.3 Peak load and associated deflection.

7.2 Energy Profiles

The energy profile provides some details of the energy absorption process. Figure 7.2.1 shows the impact energy versus the absorbed energy profiles for the flat panel, small, medium, and large arches with bolted boundary condition. There is a clear trend that as the curvature increases the maximum energy absorption increases.

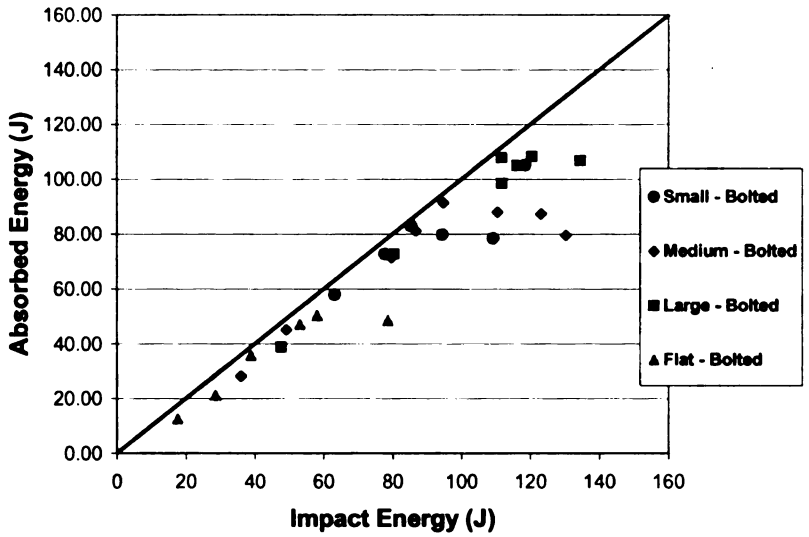

Figure 7.2.1 Energy profiles for bolted small, medium and large arch, and flat panel.

Table 7.2.1 shows the mass, maximum absorbed energy, and the ratio of them. The ratio gives an indicator of the trade-off of weight to energy absorption. The data shows that the weight increases with increasing curvature. The absorbed energy of the flat panel is about 71 Joules, the small arch 83 Joules, the medium arch 91 Joules, and the large arch 108 Joules. Looking at the ratio of the maximum absorbed energy (AE) to the mass, it can be seen that the large arch has the best energy absorption to weight ratio.

Table 7.2.1 Bolted specimens mass and maxium absorbed energy.

	Mass (g)	Max. Absorbed Energy (J)	Max. AE/Mass (J/g)
Flat Panel	42.2	50	1.19
Small	43.1	83	1.93
Medium	44.6	91	2.04
Large	47.6	108	2.27

7.3 Characteristics of Impact Response

Figure 7.3.1 shows a plot of the stiffness for the camber of the arches for all three boundary conditions. As expected, the flat panel has the highest stiffness. Despite some

scatter in the data the small arch has the lowest average stiffness for the bolted specimens. For the frame and bolted specimens the large and medium arches have overlapping ranges of stiffness, which suggest that they have similar stiffness. However, the bar clamped boundary conditions show that the medium arch has a slightly larger range of stiffness than the large arch. Since, the results from the bolted boundary condition can be considered to be most consistent it can be concluded that the flat panel has the largest stiffness, the medium and large arches have similar stiffness and the small arch the least.

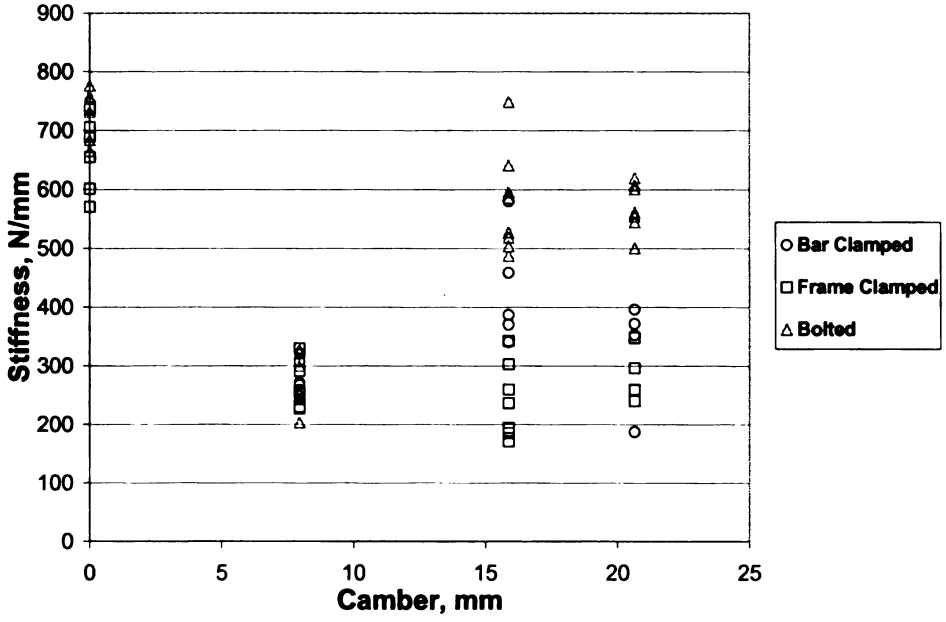

Figure 7.3.1 Stiffness as a function of camber.

Figure 7.3.2 shows a plot of camber of the arches in comparison to the peak loads. The trend are roughly linear with some scatter in the data, with the flat panel having the largest peak load, followed by the small arch, with the large arch having the smallest peak load on average. This is also noticeable in Figure 7.1.1, where the flat panel has the

largest peak force, followed by the small arch, and medium arch, and then large arch. Even though the ranges show some overlap, there is a noticeable trend in that the small arch has a higher peak load than the large arch.

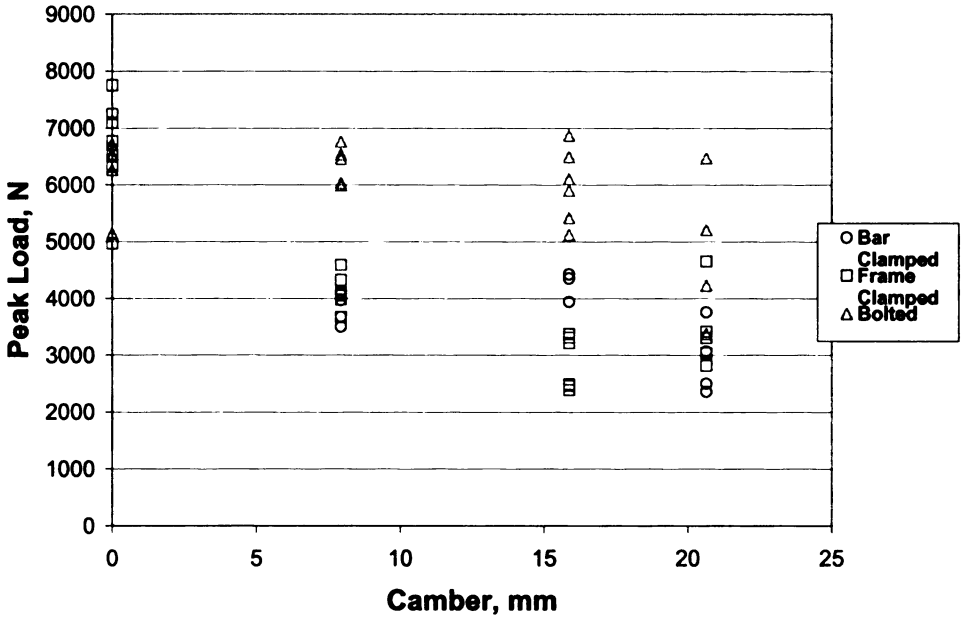

Figure 7.3.2 Peak load as a function of camber.

It is desired to study the effects curvature has on the first peak load for the bolted specimens. Figure 7.3.3 shows the first peak load compared to the arch cambers. The initial peak load decreases with decreasing curvature. From an energy and armor design standpoint the large arch would be first choice because overall it absorbs the most energy.

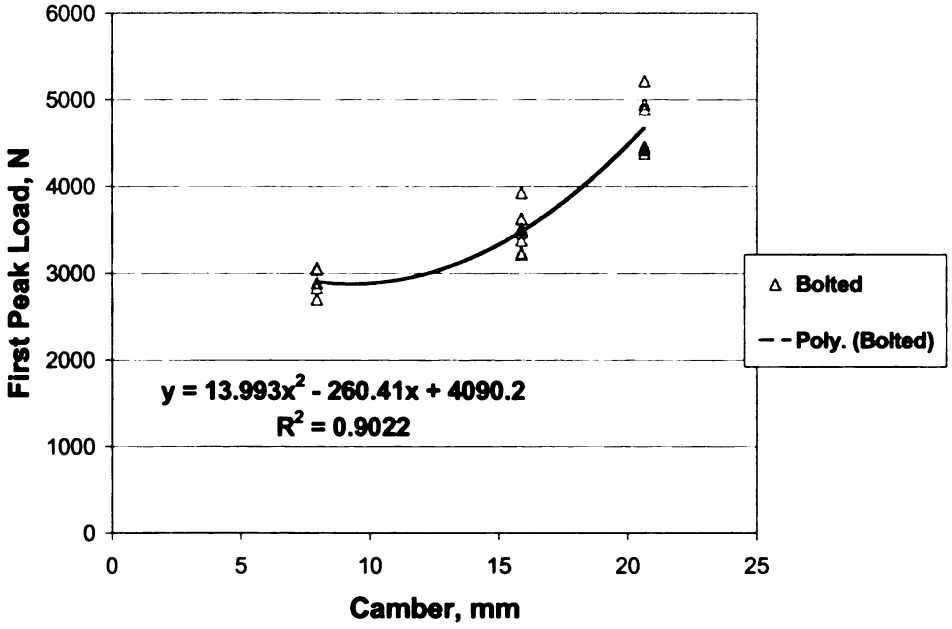

Figure 7.3.3 First peak load for bolted specimens.

Because deflection is one of the major contributors to energy absorption, the trends of the maximum deflection are plotted for each design in Figure 7.3.4. The large arch traveled the longest distance, followed by the medium, and small arches. As expected the

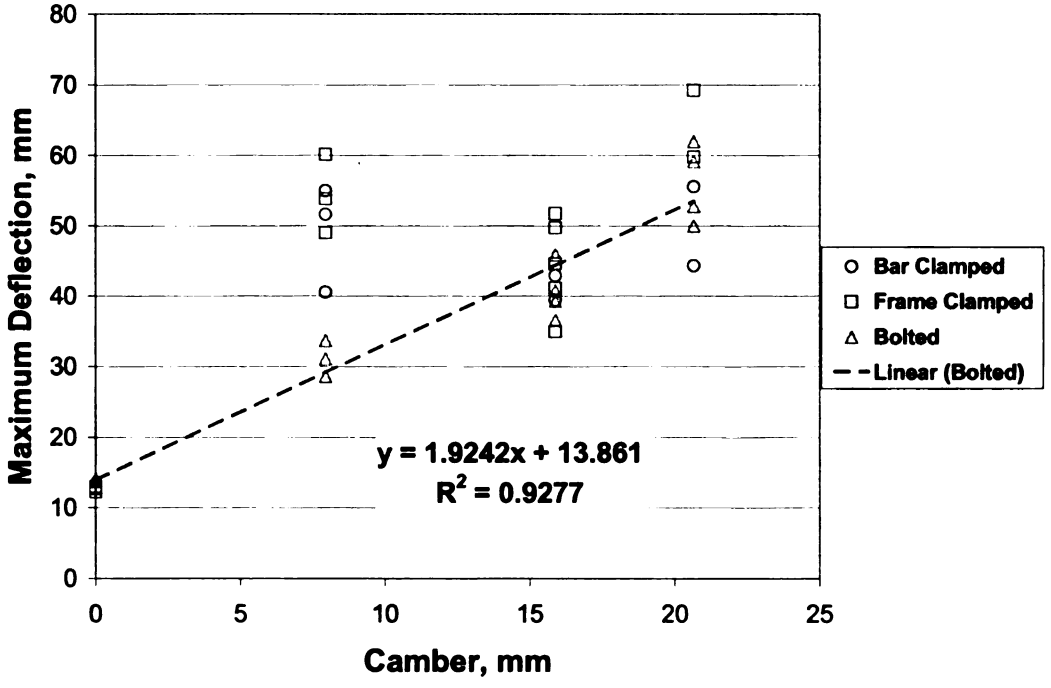

Figure 7.3.4 Maximum deflection for each arch height.

flat panel has the smallest maximum deflection. A trend line has been plotted for the bolted specimens to enhance the trend due to the camber.

The contact duration is plotted in Figure 7.3.5. The contact duration is measured only for open curves. The bar and frame clamped contact durations have a lot of scatter. The bolted specimens have less scatter in the contact time and show a linear trend with the camber.

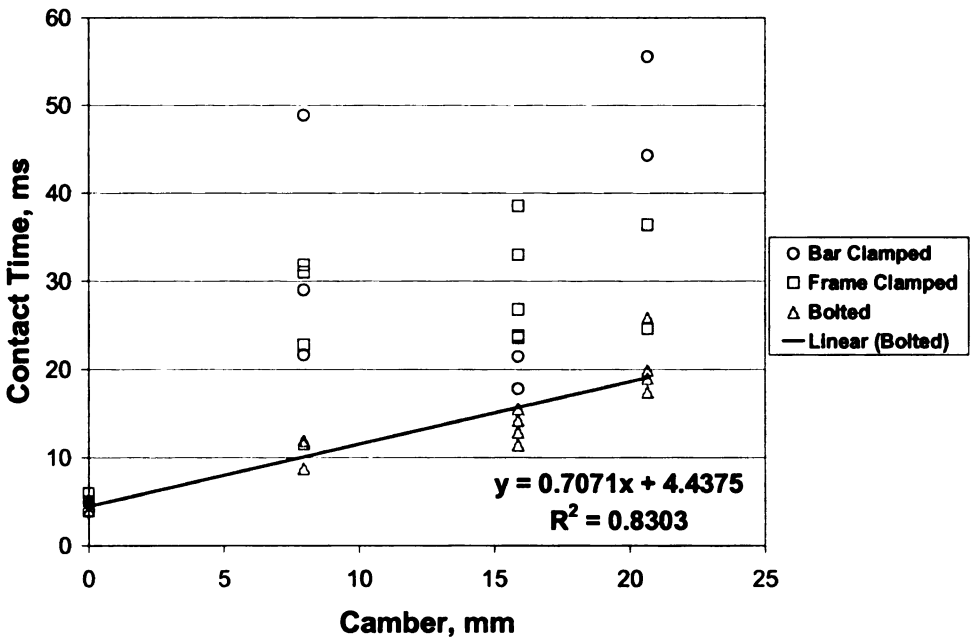

Figure 7.3.5 Contact duration for each arch height.

Table 7.3.1 below summarizes all characteristics of impact response for the bar clamped specimens with averages. The values are all averages and shown in bold font. They are followed by the standard deviations in regular font. The medium arch has the largest stiffness, with the small arch having the lowest. The medium arch has the largest peak load of 4236N, followed by the small arch with 3802N. The large arch has the lowest peak load of 2918N. The large and small aches have similar maximum deflections. The maximum deflections however, are very similar for the small and large

arch, but surprisingly the medium arch has a lower maximum deflection. The large arch has the longest contact duration. The medium arch has the shortest contact time with the small arch having a longer contact time. The large arch has the most absorbed energy, but is followed by the small arch. The medium arch specimen has the lowest absorbed energy.

Table 7.3.1 Impact characteristics for bar clamped $[0/90]_{3s}$

Arch Size	Stiffness (N/mm)	Peak Load (N)	Deflection @ peak load (mm)	Max Deflection (mm)	Contact Duration (ms)	Absorbed Energy (J)
Small	285/27	3802/265	15.9/7.5	49.0/7.5	33.2/14.1	93
Medium	427/96	4236/263	27.1/2.1	41.1/2.5	19.6/2.6	67.4
Large	327/95	2918/635	29.0/15	49.9/8.0	48.4/0.4	101.2

Table 7.3.2 shows the response characteristics for the arched composites and the flat panel for the frame clamped boundary condition. Again the initial stiffness of each arch is similar and statistically the same. The large and small arches have peak loads of 3444N and 4119N, respectively. Taking into account the large standard deviations, there is a large overlap in the data. The deflections for these peak loads do show the same trend as the bar clamped, except that there is a larger standard deviation. The maximum deflections of the specimen show a trend, except when looking at the standard deviations, which show some overlap in the results. Due to the pulling out of the clamping system the maximum deflection has large standard deviations. The contact duration is statistically the same due to the standard deviations. The small and medium arches

Table 7.3.2 Impact characteristics for frame clamped $[0/90]_{3s}$ specimens.

Arch Size	Stiffness (N/mm)	Peak Load (N)	Deflection @ peak load (mm)	Max Deflection (mm)	Contact Duration (ms)	Absorbed Energy (J)
Flat	671/65	6662/887	10.0/1.37	12.66/0.38	4.98/0.98	50.8
Small	262/40.1	4119/312	18.4/5.1	54.3/5.6	28.5/5.0	136.4
Medium	236/62	2884/466	30.8/12.6	44.4/6.7	29.1/6.5	113.6
Large	280/43	3444/713	37.2/4.5	64.5/6.7	30.5/8.3	93.5

absorbed the most impact energy, followed by the large arch. The flat panel absorbs the least amount of energy.

Table 7.3.3 shows the results for the bolted boundary condition, which eliminates large slippage. The results include a flat panel with bolted boundary conditions. It can be seen that the standard deviations are much smaller for the bolted boundary condition results than the other two boundary conditions. The large arch, however, had a large amount of variance for the second peak load. It was found that the second peak was actually smaller than the initial peak load for the large arch. It was observed that the load-deflection plots for the bolted were more consistent and these small standard deviations prove that. The stiffest arch was the large arch, but with the standard deviation the medium and large arches have similar stiffness. The second peak loads were all very close to that of the flat panel, except for the large arch. Again, with the large standard deviations there is statistically no difference. The deflection at the peak loads has very small standard deviations, where the large arch has a peak load at 47.4mm on average. The medium arch has its peak load at 32.4mm and the small at 21.9mm. That is nearly a 10mm difference for each arch design. The maximum deflections show a similar trend. The contact duration shows this trend where contact time increases with curvature. The energy absorption increases with increasing curvature, where the energy absorption increase from 50.5J for the flat panel to 107.8J for the large arched composite.

Table 7.3.3 Impact characteristics for bolted $[0/90]_{3s}$ specimens.

Arch Size	Stiffness (N/mm)	First Peak Load (N)	Second Peak Load (N)	Deflection @ max load (mm)	Max Deflection (mm)	Contact Duration (ms)	Absorbed Energy (J)
Flat	**728**/44	-	**6309**/596	**9.0**/1.45	**13.8**/0.23	**4.7**/0.65	**50.4**
Small	**276**/49	**2904**/150	**6294**/333	**21.9**/1.1	**31.3**/2.5	**10.8**/1.7	**83.02**
Medium	**576**/87	**3488**/221	**5984**/653	**32.4**/1.1	**40.6**/3.9	**13.5**/1.8	**91.3**
Large	**570**/42	**4628**/399	**4702**/1182	**47.4**/2.0	**56.6**/5.5	**20.5**/3.7	**107.8**

7.4 Summary

By adding various curvatures together or choosing an optimum curvature the most energy can be absorbed. The large curvature absorbs the most energy and from the load deflection relation it is apparent that it is the large deflection. When looking at the bolted boundary condition the medium and large arches have similar stiffness, but the small arch has the lowest stiffness. In regards to the peak load and its deflection the less curvature the higher the load and the less deflection. There is a linear relation between curvature and maximum deflection. With the larger deflection comes a slightly longer contact time.

For energy absorption the best boundary condition is the frame clamped. The frame clamped specimens have some slippage, which allows increased energy absorption. The down side with the frame clamped boundary condition is inconsistence results. The bolted specimens have low standard deviations and predicable results. The bolted results show the trends in impact results for each curvature.

8. BUCKLING AND DAMAGE PROCESS

8.1 Buckling process literature review

The damage and buckling processes for arched composites was complex and can easily be the focus of a research project. The buckling process and damage have been studied by Wardle [28] in his work on composites shells (arches). His work on bifurcation buckling provided a definition of buckling for bolted arched composites. He focused on quasi-static loading and modal analysis after damage to define buckling. He defined limit-point buckling to be the point on a load-deflection curve where the tangent stiffness slope goes to zero. This is when the load peaks and then drops off. A characteristic of bifurcation buckling is when there is a discontinuity in the tangent stiffness slope, but is usually identified by the tangent stiffness slope becoming negative. He said that buckling is the process of compressive membrane strain energy transferring to bending strain energy. In work by Ciu, et al. [4] for quasi-static loading of dome composite shells, defined bifurcation buckling when the center deflection buckled away from the platen surface. The dome initially formed a flat surface with the platen surface, and after more loading it formed a dimple or inverted the center away from the platen surface. Buckling was at the point when this dimple was formed. This happened when there was a decrease in the loading per platen deflection. This agrees with Wardle [28] where he later stated that bifurcation buckling in pressure loaded spherical caps is found by a change in the tangent stiffness slope, but the slope remained positive. Analytical work has shown that positive Gaussian curvatures (arches) are shear buckling resistant apposed to shells with negative (peaks & valleys in the arch) or zero (flat plat) Gaussian curvature [17].

In the damage process work by Huang et al. [9] on static contact crushing of arched composites showed the buckling and damage phenomena. It was observed that cracking near the peak of the arch almost split the specimen into two pieces. Other work by Johnson and Holzapfel [30] showed the extensive delamination damage and transverse cracking of an arched composite impacted at speeds of 107.5 m/s. The delamination area was large, extending from the impact location and partially down the sides and to the edges near the peak.

8.2 Buckling Process

The damage process is a very complex phenomenon, which can be roughly represented by the schematics shown in Figures 8.2.1, 8.2.2, 8.2.3. Each figure shows a single load-deflection curve that is representative of a damaged specimen. The energy-deflection relation is also plotted. The curve is marked by six critical points in the process, lettered A through F. Next to each load-deflection curve is a scaled schematic showing the buckling and bending of the specimen during the impact process. Each schematic begins with the initially undamaged specimen, followed by the damaged specimen at deflection points B-F, where the deflection of the center of the specimen is the only known point. The deformed profiles were created with resemblance to Wardle's quasi-static loading results. Initially, each specimen is in its original undamaged state point A. Then the composite is impacted and the load rises to point B. The load then drops from point B to point C with very little deflection. The critical buckling load or onset of buckling is at point B. The specimen then deflects to the point where it ends up in an inverted state, which occurs at point D. The peak of this load is at point E where the specimen is either in a completely inverted

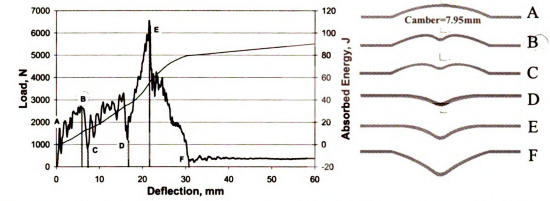

Figure 8.2.1 (a) Common bolted small arch load-deflection curve (b) Schematic of specimen buckling and deflection at critical points.

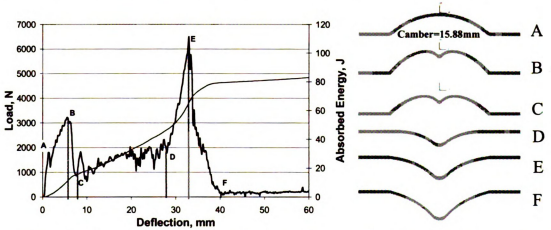

Figure 8.2.2 (a) Common bolted medium arch load-deflection curve (b) Schematic of specimen buckling and deflection at critical points.

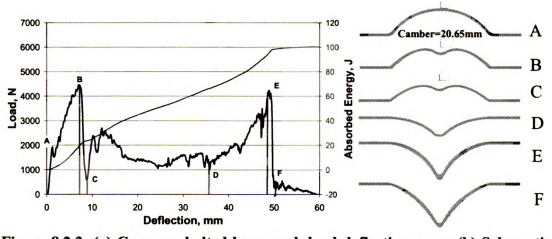

Figure 8.2.3 (a) Common bolted large arch load-deflection curve (b) Schematic of specimen buckling and deflection at critical points.

state (twice the original height of the arch) or in a hyper-inverted (more than twice the original height of the arch). At point F, all specimens will be in a hyper-inverted state because enough delamination and fiber breakage has taken place allowing the specimen to deflection beyond twice the original height of the arch.

During the impact process, the tip of the tup did not typically penetrate the specimen. Perforation would take place when the arch had collapsed and inverted. When perforation did take place, the tup tip left a hole at the center of the specimen or enough delamination, matrix cracking, and fiber breakage across the width of the specimen caused the composite to break into two pieces. More commonly, the specimen would pull out of the clamps before perforation; however, the bolted design eliminated the pullout and increased the amount of damage in the specimen.

To compare the deflection of the arch peak during the impact process, the values from the critical values on the plots in Figures 8.2.1, 8.2.2, and 8.2.3 are plotted in a single

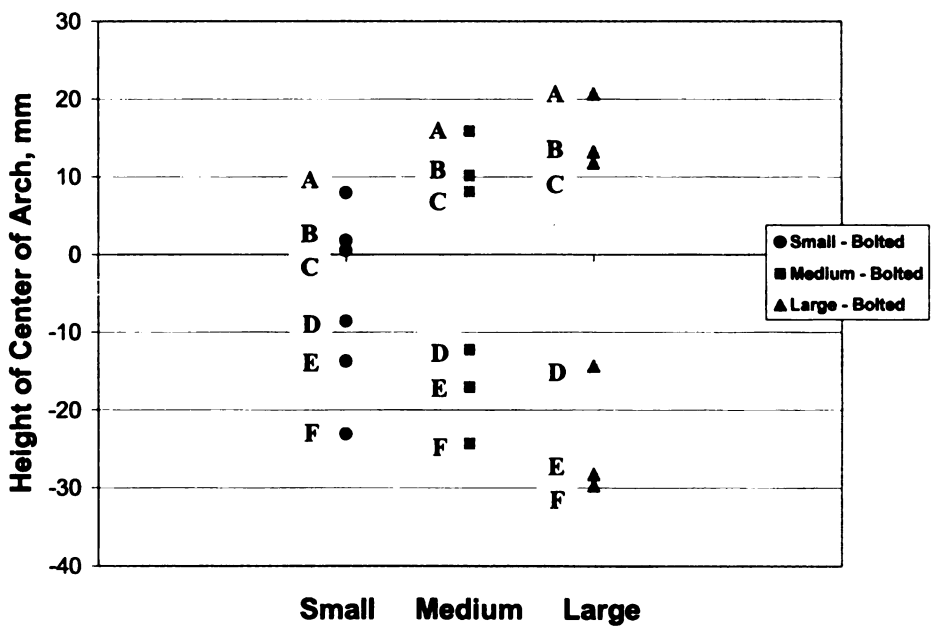

Figure 8.2.4 Deflection of small, medium, and large arch peaks during impact.

chart. Figure 8.2.4 shows this plot where the arch sizes are plotted on the abscissa and the height of the center of the arch is plotted on the ordinate. The data points labeled A are the initial height of each arch before damage. The other five points are the critical deflection points B through F. It can be seen that the initial maximum load at deflection B occurs at roughly the same amount of deflection. The onset of buckling takes place at point B. At point C each specimen goes through a large deflection with low loading. This deflection difference from C to D increases with the arch camber. It can be seen that the large arch has the largest overall deflection and inverts to over –30mm and the medium to –24 and the small to –22mm. Clearly, the deflection after onset of buckling to point D is a main contributor to energy absorption because of the specimen's distance traveled. This can be seen in by the energy-deflection relation plotted in Figures 8.2.1, 8.2.2, 8.2.3.

8.3 Damage Process for flat panel composite

The damage process is much different for a conventional flat panel than a arched composite. In particular, the final damage is much different. Figure 8.3.1 shows a bottom view of a bolted flat panel on a light table, where perforation was reached. Local

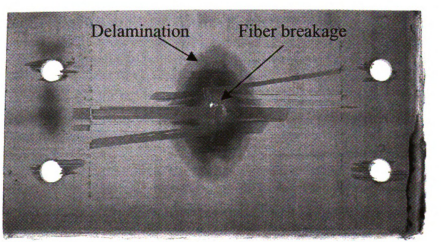

Figure 8.3.1 Bottom view of $[0/90]_{3s}$ of bolted flat panel.

delamination can be seen near the impact point. There is also fiber breakage and some fiber pullout and strips of delamination on the backside. The main cause for the delamination is the fiber angle difference between adjacent layers causing interlaminar shear stresses.

The top view of this specimen can be seen in Figure 8.3.2. Again, it is on a light table, but due to the protruding damage on the backside it cannot lay directly on the table, which causes the darker colors. The most noticeable damage is that the fibers have been pushed from the top layers through the hole. Once again, it can be seen that the damage is local to the hole and that there is less damage on the impact side.

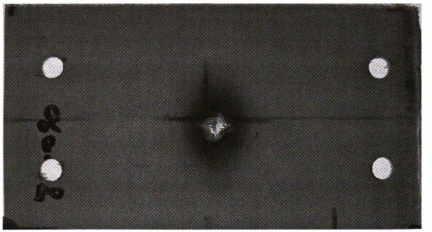

Figure 8.3.2 Top view of $[0/90]_{3s}$ bolted flat panel.

The frame clamped flat panels produced some expected results. The main difference between the frame clamped and bolted boundary conditions was that there was increased bending of the specimen for the frame clamped. This bending allowed more fiber breakage along the transverse direction. Figure 8.3.3 shows a bottom view of a frame clamped flat panel on a light table. The damage near the impact location is now elongated in the transverse direction due to the bending of the specimen. Fibers now break not just due to the localized loads at the impact point, but also in regards to the

bending of the specimens. This bending also causes the fibers on the bottom side to be pulled in tension and break. There is some localized delamination around the parameter of the broken fibers and some more wide spread delamination on the upper left side.

Figure 8.3.3 Bottom view of $[0/90]_{3s}$ frame clamped flat panel.

A top view can be seen in Figure 8.3.4 for the frame clamped specimen. The delamination area looks even smaller than the bottom view. Again the hole where the tup tip perforated the specimen can be seen with the transverse elongation of damage. The damage does not spread along the axial direction as much as the transverse.

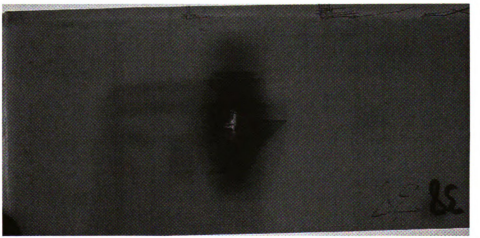

Figure 8.3.4 Top view of $[0/90]_{3s}$ frame clamped flat panel frame.

8.4 Damage process for arched composite

Fiber breakage and delamination traveled the top of each specimen in the transverse (90°-direction) direction. The fiber breakage was visible at the initial stages of damage, where it began at the free edges and propagated towards the center. The fiber breakage began at the top surface and worsened as the delamination became more pronounced. Figure 8.4.1 shows an oblique side view of a damaged composite. The delamination and fiber breakage near the top surface can be easily seen. Notice how the top layers are completely fractured along the width of the specimen.

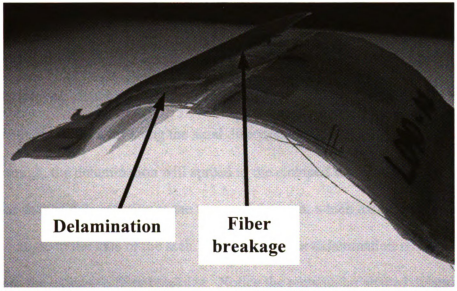

Figure 8.4.1 Side view of damaged bolted $[0/90]_{3s}$ large arch composite.

Figure 8.4.2 shows a top view of the specimen in Figure 8.4.1. Faint changes in the shades of the color show the delamination patterns on the top of the specimen. The fiber breakage along the transverse direction can be seen. The side view shows more of the extensive damage.

Figure 8.4.2 Top view of damaged bolted $[0/90]_{3s}$ large arch composite.

A top view of a damaged frame clamped specimen can be seen in Figure 8.4.3. It is on a light table, which shows the delamination patterns. The delamination is in oval patterns with the major axes along the axial direction (0°-direction). If the impact energy is great enough, the delamination will spread to the clamped wings. There is also rectangular shaped delamination at the center of the arch, which extends to the edges at an oblique angle to the axis of the arch. This rectangular delamination is able to take place due to the extensive fiber breakage. Notice the rectangular shaped delamination area near the transition from the arch to the winged sections. This delamination takes place due to the bending of the sides. For the bolted specimens the delamination near the top center and from the bending of the sides meets causing complete delamination of the layers. As the specimen buckles the damage progressively increased by delamination and fiber breakage in the layers at the peak of the arch.

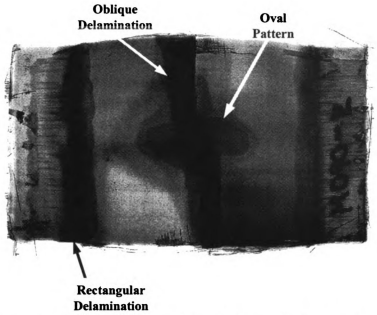

Figure 8.4.3 Top view of delamination of $[0/90]_{3s}$ frame clamped medium arch showing delamination pattern.

8.5 Summary

In order to understand how the energy is absorbed the buckling and damage process must be studied. Buckling typically increases the complexity and instability of the damage process creating less predictability and difficulty in characterizing the damage. If buckling is reduced more control over the specimen damage process will allow precise damage control, which in turn will allow control in energy absorption. In our work, it was believed that buckling occurred more apparently in the specimens with the bolted boundary condition due to the specimen being unable to slip. Frame clamping would allow the specimen to smoothly bend during impact. The slipping of the specimen at the clamping boundaries allowed the specimen to bend and deflect downward, without large drops in load, which are associated with buckling. By bolting the specimen, the boundaries were fixed, forcing the specimen to suddenly fail, which is apparent by sudden load drops. The peak load before this sudden load drop is the onset of buckling.

Bolting the specimen increased the visible delamination and fiber breakage and several times the specimen actually broke into two pieces because of the high impact energy.

9. CONCLUSIONS AND FUTURE STUDY

9.1 Conclusions

The main goal of this study was to determine the effects of curvature on energy absorption. The trend was clearest for the bolted boundary condition. As the curvature increased the maximum absorbed energy increased. From the load-deflection relation it became apparent that the large deflection of the specimens contributed to the energy absorption. With increasing curvature came increasing camber and ultimately larger deflection of the specimen.

In the beam and plate problem, the beam clearly absorbs more energy without breaking. The trade off is that it has lower stiffness and larger deflection. The beam is 25.6% less stiff than the plate, but absorbs nearly 50% more energy without as much damage. The deflection is the main contribution of the energy absorption because the maximum deflection is almost twice in the beam for the doubling of energy absorption. This is only the case because the peak load is slightly lower in the beam case. It is likely that the friction forces around the clamped boundaries decrease deflection of the specimen, but increases the peak loads. The clamping boundary forces are critical to prevent slippage, which would allow for increased energy absorption. But the beams can deflect more than the plate due to the free boundary on the two sides.

For the boundary condition effects for the arched specimens, the most noticeable feature is that the bolted arched specimens have the largest peak load. The small arch has the largest peak load with the large arch with the smallest peak load. The frame clamped boundary condition has the largest maximum deflection for each arch size. This large deflection is one of the contributing factors to energy absorption.

The large curvature absorbs the most energy and from the load deflection relation it is apparent that it has the largest deflection. When looking at the bolted boundary condition the medium and large arches have similar stiffness, but the small arch has the lowest stiffness. In regards to the peak load and its deflection the less curvature the higher the load and the less deflection. There is a linear relation between curvature and maximum deflection. With the larger deflection comes a slightly longer contact time.

For energy absorption the best boundary condition is the frame clamped. The frame clamped specimens have some slippage, which allows increased energy absorption. The down side with the frame clamped boundary condition is inconsistence results. The bolted specimens have low standard deviations and predicable results. The bolted results show the trends in impact results for each curvature.

In order to understand how the energy is absorbed the buckling and damage process was be studied. Buckling typically increased the complexity and instability of the damage process creating less predictability and difficulty in characterizing the buckling. If buckling is reduced more control over the specimen damage process will allow precise damage control, which in turn will allow control in energy absorption. It is believed that buckling occurred in the specimens with the bolted boundary condition due to the specimen being unable to slip. Slippage would have allowed the specimen to smoothly bend during impact. The slipping of the specimen at the boundaries allows the specimen to bend and deflect downward, without large drops in load. By bolting the specimen, the boundaries were fixed, forcing the specimen to suddenly fail, which is apparent by sudden load drops. This sudden load drop is the onset of buckling. Bolting the specimen

increased the visible delamination and fiber breakage and several times the specimen actually broke into two pieces because of the high impact energy.

In a book by Ashby, et al. [32] on metals foams it is apparent that the load-deflection relation for these foams is similar to the relation for arched composites. There is an initial peak load, similar to the frame clamped initial peak. The load then dips slightly and remains constant while the foam collapses. As near the end of the densification of the foam the impact load increases sharply. This sharp increase is similar to the bolted specimens in the inverted state. An arched polymer matrix composite could be a replacement for metal foams.

Photos of the damaged specimens are in the appendix. The photos are given in two columns with the top view on the left and bottom view on the right. The damage type of each specimen in listed in corresponding tables. If a specimen is perforated it is designated with a P, non-perforated with NP, and broken in two pieces with BITP.

9.2 Future Study

The literature review and this study consisted of impacts on the arch peaks and normal to the surface. A thorough study of the effects of oblique and off peak impacts will provide a complete analysis of the curvature effects on impact characteristics. This study will show the usefulness of arched composites in armor design, where direct impacts are not always the case. The main variable in this study was the camber, which was varied by changing the radius of curvature and maintaining the span of the arch at 7.62cm (3.0"). In studying curvature the effects of span of the arch and the length of the arch are important. It may be desirable to maintain a constant camber, by changing the radius of

curvature and allow the arch span to vary. This study will be very insightful because the camber appears to be a major contributor to energy absorption.

Low speed impact tests have been conducted, but ballistic and blast tests produce different results in polymer matrix composites. A couple ballistic tests on the arched composites in a shock tube showed large delamination. It is believed that an arched composite will absorb more ballistic energy than a flat panel due to the spread of damage.

APPENDICIES

APPENDIX A

MATLAB code for producing extension method line and calculating impact energy and absorbed energy

```
clear all
clc
%%%%%%%%%%%%%%%%%%%%%%%%%%%%%%%%%%%%%%%%%%%%%%%%%%%%%%%%%%%%%%%%%%%%%%%
%   This program is written for English units (ft, lb, s)    %
%%%%%%%%%%%%%%%%%%%%%%%%%%%%%%%%%%%%%%%%%%%%%%%%%%%%%%%%%%%%%%%%%%%%%%%

%Import EXCEL with xlsread('File_Name.xls','XLS_Worksheet')
data = xlsread('Dynatup Data.xls', 'Raw_Data');

%Organizes EXCEL data into MATLAB vectors
Point_Number = data(:,1);
Time = data(:,2)/1000;
Load = data(:,3);
Deflection = data(:,4)/12;
Velocity = data(:,5);
Energy = data(:,6);

%Asks user to specify whether or not the particular impact
%test was a REBOUND curve or an open PENETRATION curve.
r=input('Rebound enter 1 OR Penetration enter 0');

%Input the weights of the crosshead, tup, tup bolt, and additional
weights
weight=27.07; %lbs


Mass = weight/32.1740;

%Finds the velocity at initial impact.
l=0;
for(i=1:length(Time));
    if(Time(i)==0);
        l=l+1;
        zero_velocity(l) = Velocity(i);
    end
end

if r==1
    h=max(Deflection); %Finds h' for rebounding results
%Calculates the extension and adds additional data points
%to the existing vectors to create the extension.
elseif r==0
u=10; %No. of data points to generate trendline from.
a=length(Deflection);
c=Deflection(a-u:a);
d=Load(a-u:a);
p = polyfit(c,d,1); %Fits a trendline through data to determine
%extension slope.

xmax=-p(2)/p(1);    %Determines where the extension intersects the x-
axis.
del=(xmax-Deflection(a))/10; %The delta increments from the first
extension
```

```
%data point to the data point on the x-axis.  There are 10 points in
this
%range.

%Adds the extended data points to the Load & Deflection vectors.
for i=1:10
Deflection(a+i)=Deflection(a)+(del*i);
Load(a+i)=Deflection(a+i)*p(1)+p(2);
end
h=xmax;
end


Impact_Energy = .5*Mass*zero_velocity.^2 + Mass*32.174*h
Absorbed_Energy_polyarea=polyarea(Deflection,Load)
Energies=[Impact_Energy Absorbed_Energy_polyarea]

figure (5)
plot(Deflection, Load)
```

APPENDIX B

Flat specimens with two sides frame clamped for plate versus beam impact study

(hot press cured)

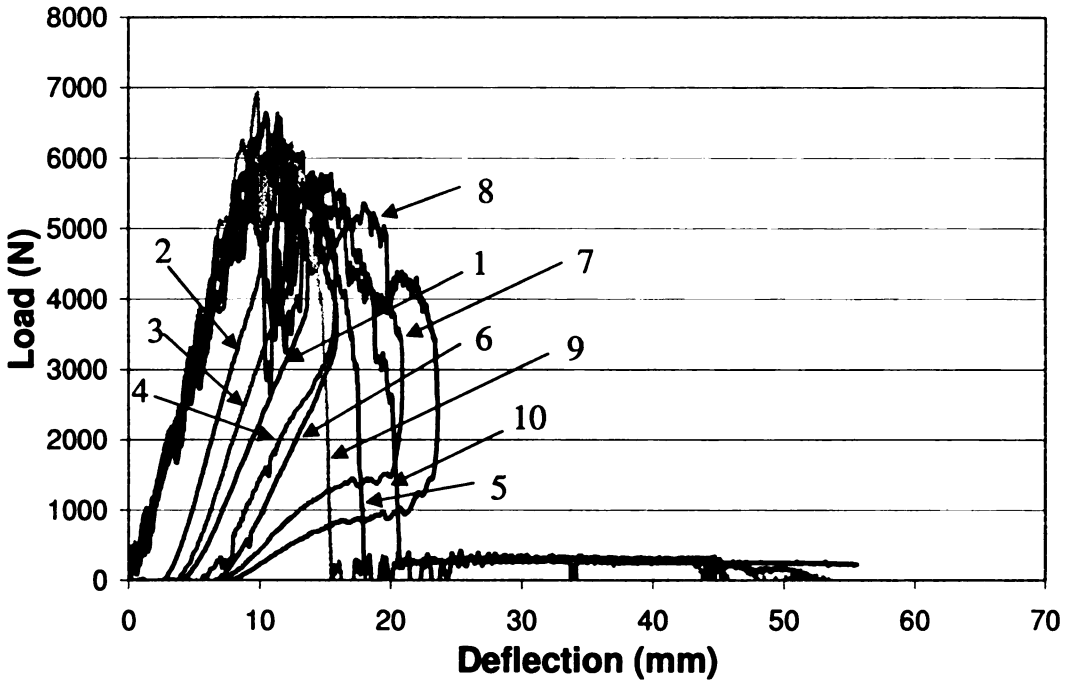

Figure B.1 Load-deflection curves for flat beam with two sides frame clamped.

Table B.1 Flat panel (beam) data.

Specimen #	Stiffness 1 (N/mm)	Stiffness 2 (N/mm)	Peak Load (N)	Deflection @ peak load (mm)	Max Deflection (mm)	Contact Duration (ms)
1	579	461	5925	12.0		
2	564	610	5639	10.2		
3	610	544	6552	11.6		
4	564	543	5734	13.7		
5	655	572	6629	10.5	18.0	6.6
6	647	551	6051	10.5		
7	651	749	5600	8.3		
8	591	634	5978	9.4		
9	690	590	6929	9.9	20.8	7.1
10	649	585	6571	11.5	15.4	4.6
Average	620	584	6161	10.8	18.1	6.1
Std. Dev.	44	75	472	1.52	2.70	1.31

Table B.2 Flat panel (beam) Energy data.

Specimen #	Impact Energy (J)	Absorbed Energy (J)	Damage
1	48.6	31.5	NP
2	29.8	14.0	NP
3	44.6	26.7	NP
4	58.5	42.2	NP
5	78.5	71.5	P
6	62.4	49.0	NP
7	78.9	65.4	NP
8	90.4	79.2	NP
9	87.4	61.1	P
10	95.1	82.8	P

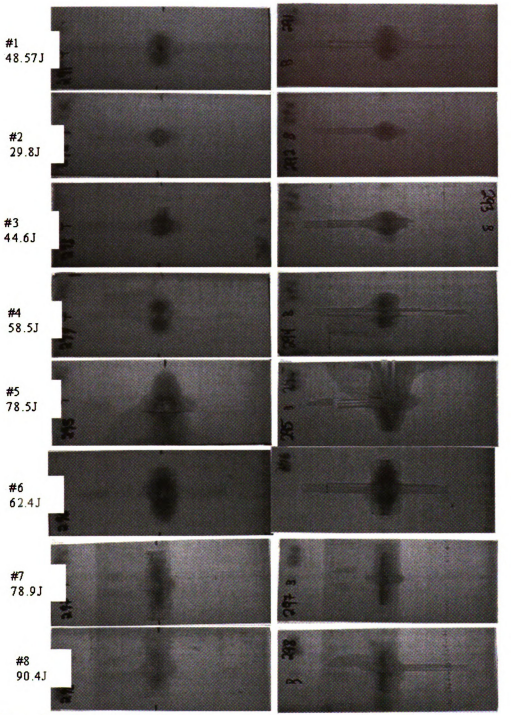

Figure B.1 Flat panel (beam) damaged specimen photos.

Note: Specimen #1 had multiple hits.

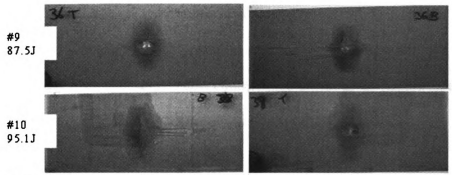

Figure B.2 Flat panel (beam) damaged specimen photos.

APPENDIX C

Flat specimens with four sides frame clamped for plate versus beam impact study

(hot press cured)

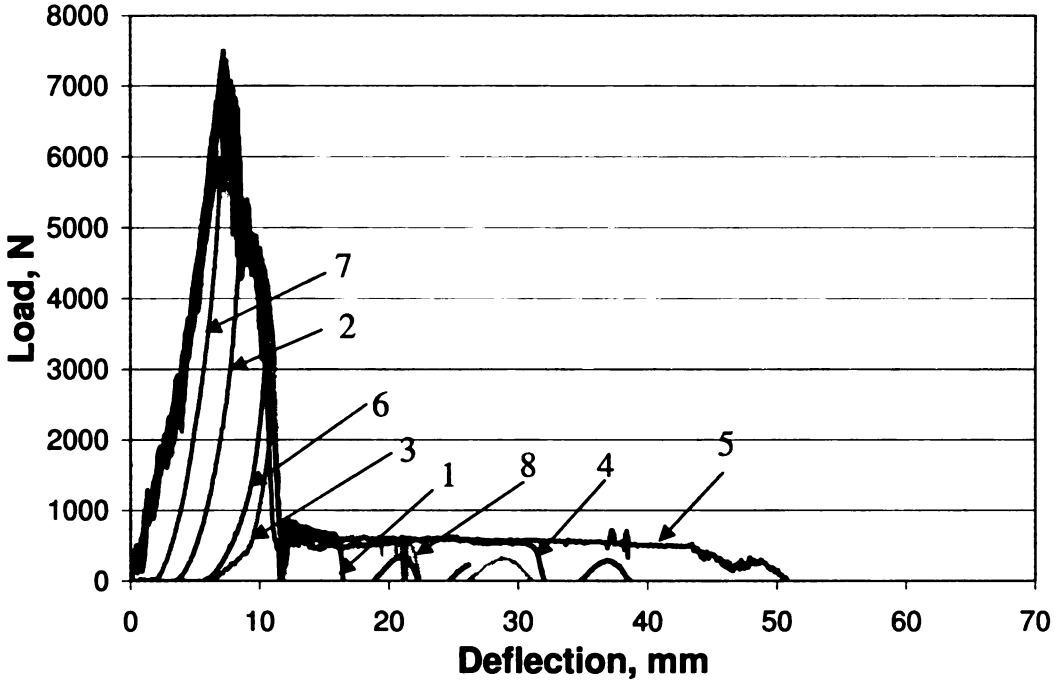

Figure C.1 Load-deflection curves for flat plate four sides frame clamped.

Table C.1 Flat panel (plate) data.

Specimen #	Stiffness 1 (N/mm)	Stiffness 2 (N/mm)	Peak Load (N)	Deflection @ peak load (mm)	Max Deflection (mm)	Contact Duration (ms)
1	968	1386	7227	7.37	11.82	5.00
2	723	1194	7224	7.52		
3	921	1469	7496	7.25		
4	834	1219	6218	7.81	11.98	4.57
5	914	1415	7294	7.08	11.60	3.70
6	799	1370	7035	7.47		
7	645	1182	5966	6.91		
8	864	1431	7113	7.33	12.03	4.10
Average	834	1333	6947	7.3	11.9	4.3
Std. Dev.	108	116	548	0.27	0.19	0.56

Table C.2 Flat panel (plate) energy data.

Specimen #	Impact Energy (J)	Absorbed Energy (J)	Damage
1	42.6	39.6	P
2	29.7	22.2	NP
3	42.0	38.7	NP
4	44.3	38.5	P
5	65.1	39.8	P
6	37.3	33.0	NP
7	17.7	8.2	NP
8	49.2	39.4	P

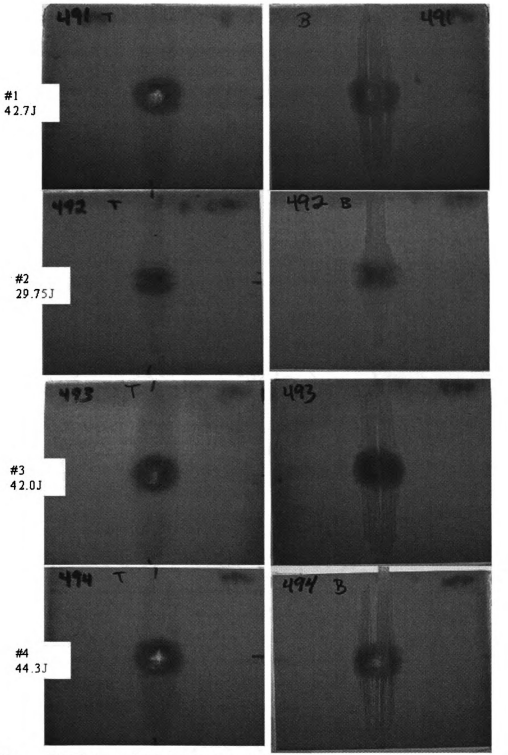

Figure C.2 Flat panel (plate) damaged specimen photos.

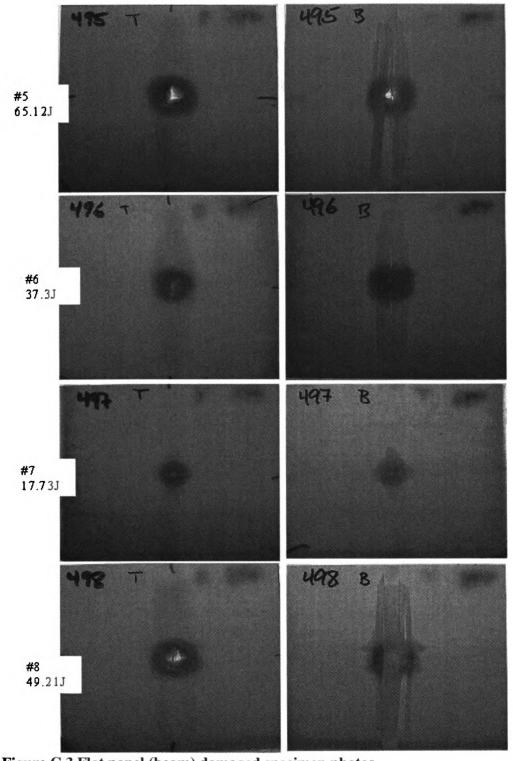

Figure C.3 Flat panel (beam) damaged specimen photos.

APPENDIX D

Flat specimens bolted (hot press cured)

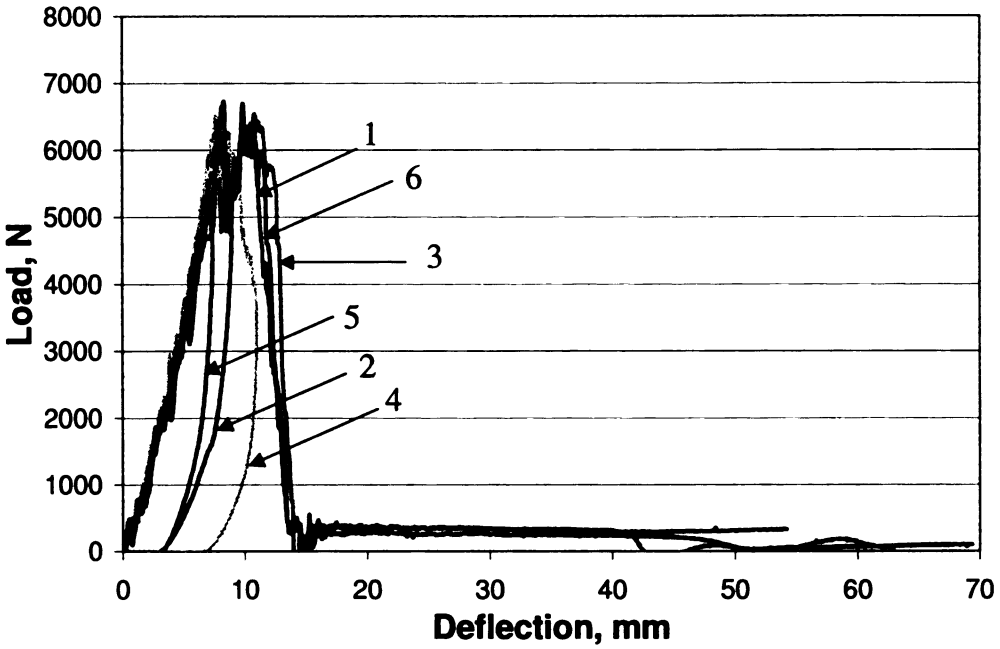

Figure D.1 Load-deflection curves for bolted flat specimens.

Table D.1 Bolted flat panel data.

Specimen #	Stiffness 1 (N/mm)	Stiffness 2 (N/mm)	Peak Load (N)	Deflection @ peak load (mm)	Max Deflection (mm)	Contact Time (msec)
1	732	852	6260	10.13	13.7	5.2
2	684	706	6722	8.354		
3	758	863	6536.92	10.832	14.09	4.9
4	776	924	6498.46	7.66		
5	665	580	5139.5	7.3		
6	754	944	6694.73	9.904	13.7	3.95
Average	728.17	811.50	6308.60	9.03	13.83	4.68
Std. Dev.	44.27	140.87	596.21	1.45	0.23	0.65

Table D.2 Bolted flat panel energy data.

Specimen #	Impact Energy (J)	Absorbed Energy (J)	Damage
1	53.1	47.1	P
2	28.6	21.2	NP
3	58.0	50.4	P
4	38.8	35.7	NP
5	17.6	12.6	NP
6	78.6	48.6	P

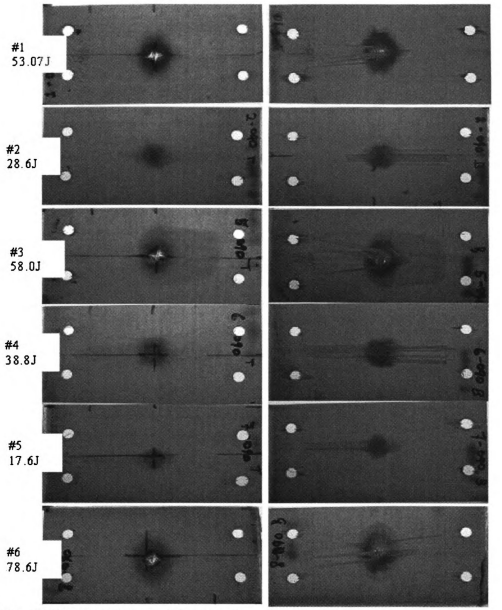

Figure D.2 Bolted flat panel damaged specimen photos.

APPENDIX E

Flat specimens frame clamped (autoclave cured)

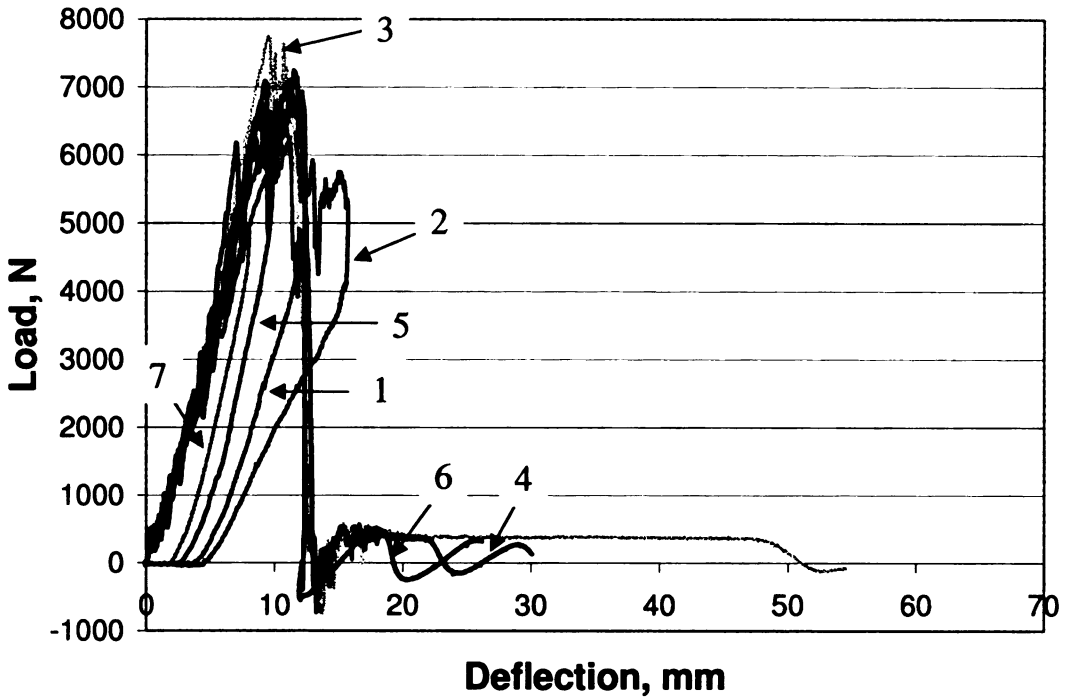

Figure E.1 Frame clamped flat panel load-deflection curves.

Table E.1 Frame clamped flat panel data.

Specimen #	Stiffness 1 (N/mm)	Stiffness 2 (N/mm)	Peak Load (N)	Deflection @ peak load (mm)	Max Deflection (mm)	Contact Time (msec)
1	570	648	6323	11.57		
2	705	683	6509	10.86		
3	736	1037	7744	9.49	12.73	4.00
4	737	851	7087	9.24	13.00	5.00
5	690	1290	6764	9.00		
6	655	804	7243	11.51	12.25	5.95
7	601	724	4963	8.00		
Average	671	863	6662	9.95	12.66	4.98
Std. Dev.	65	229	887	1.37	0.38	0.98

Table E.2 Frame clamped flat panel energy data.

Specimen #	Impact Energy (J)	Absorbed Energy (J)	Damage
1	43.1	25.7	NP
2	63.3	41.5	NP
3	61.5	50.8	P
4	61.5	50.8	P
5	34.6	19.6	NP
6	46.9	46.7	P
7	19.3	7.9	NP

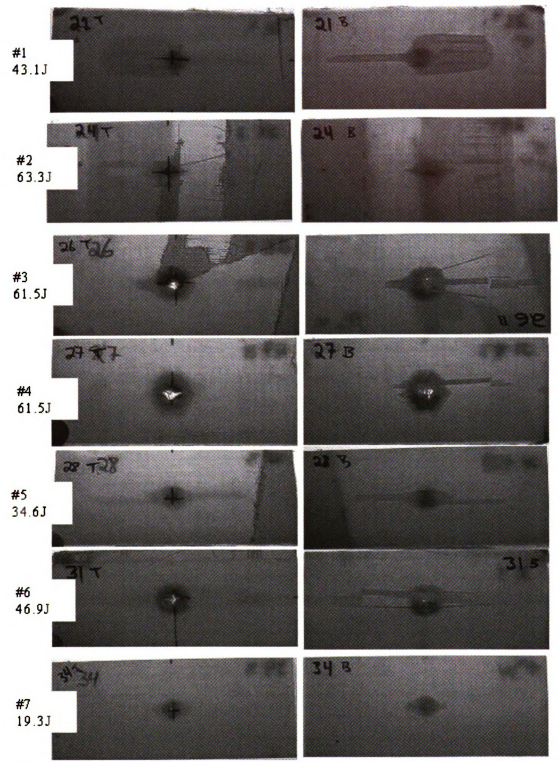

Figure E.2 Frame clamped flat panel damaged specimen photos.

APPENDIX F

Small arch with bar clamped boundary condition

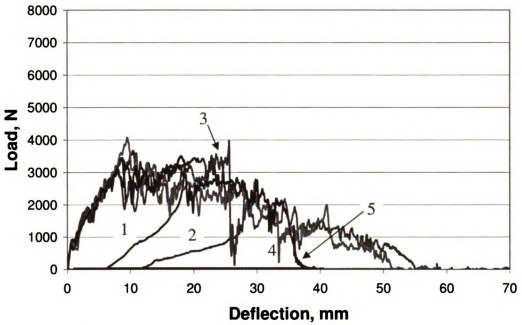

Figure F.1 Bar clamped small arch load-deflection curves.

Table F.1 Bar clamped small arch energy data.

Specimen #	Impact Energy (J)	Absorbed Energy (J)	Damage
1	44.7	32.1	P
2	74.9	65.5	P
3	109.8	64.4	P
4	96.7	93.0	NP
5	85.5	85.2	NP

Table F.2 Bar clamped small arch data.

Specimen #	Stiffness (N/mm)	Peak Load (N)	Deflection @ peak load (mm)	Max. Deflection (mm)	Contact Time (msec)
1	267	3499	18.08	40.56	48.85
2	259	3671	10.40	51.58	28.98
3	270	3966	25.61	54.99	21.62
4	320	4075	9.50		
5	307				
Average	285	3803	15.90	49.04	33.15
Std. Dev.	27	265	7.53	7.54	14.09

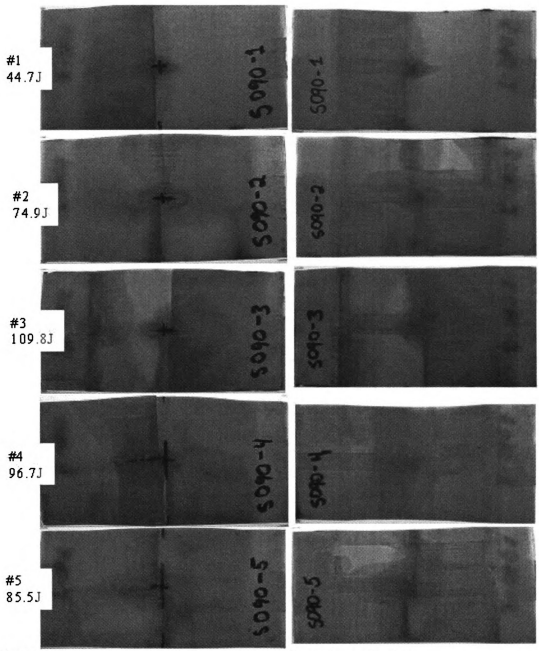

Figure F.2 Bar clamped small arch damaged specimen photos.

APPENDIX G

Medium arch with bar clamped boundary condition

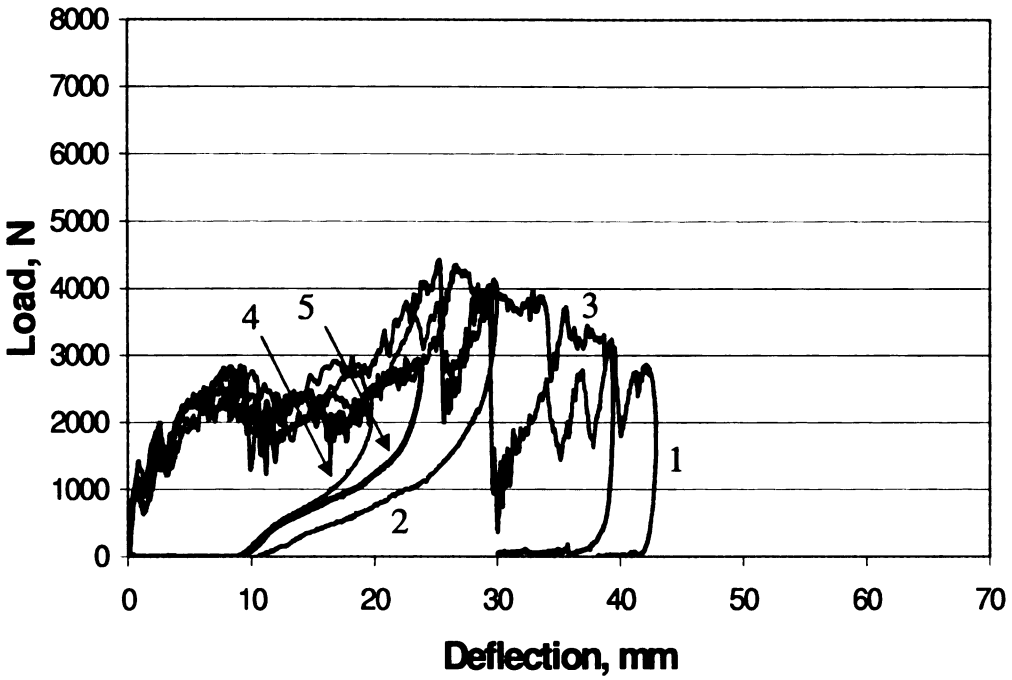

Figure G.1 Bar clamped medium arch load-deflection curves.

Table G.2 Bar clamped medium arch data.

Specimen #	Stiffness (N/mm)	Peak Load (N)	Deflection @ peak load (mm)	Max. Deflection (mm)	Contact Time (msec)
1	341	4423	25.33	39.40	17.78
2	387	4350	26.69		
3	370	3936	29.40	42.89	21.45
4	580				
5	459				
Average	427	4236	27.14	41.15	19.62
Std. Dev.	96	262	2.07	2.47	2.60

Table G.1 Bar clamped medium arch energy data.

Specimen #	Impact Energy (J)	Absorbed Energy (J)	Damage
1	108.3	64.7	P
2	74.1	55.9	NP
3	93.3	67.4	P
4	44.9	42.3	NP
5	62.4	50.7	NP

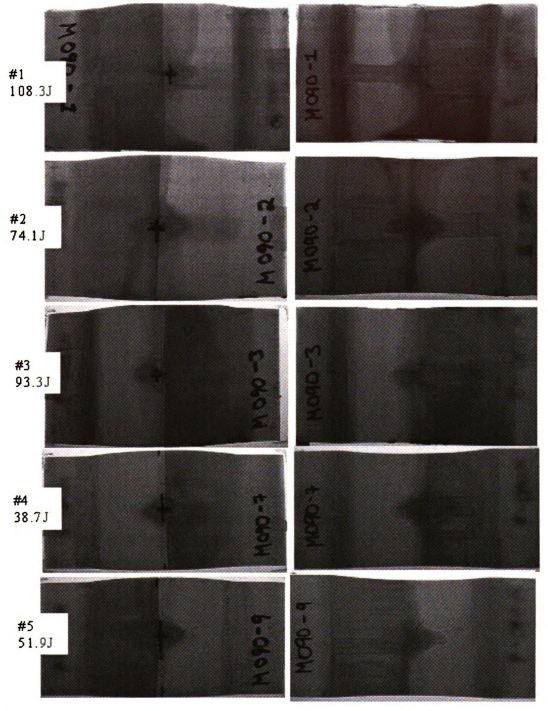

Figure G.2 Bar clamped medium arch damaged specimen photos.

APPENDIX H

Large arch with bar clamped boundary condition

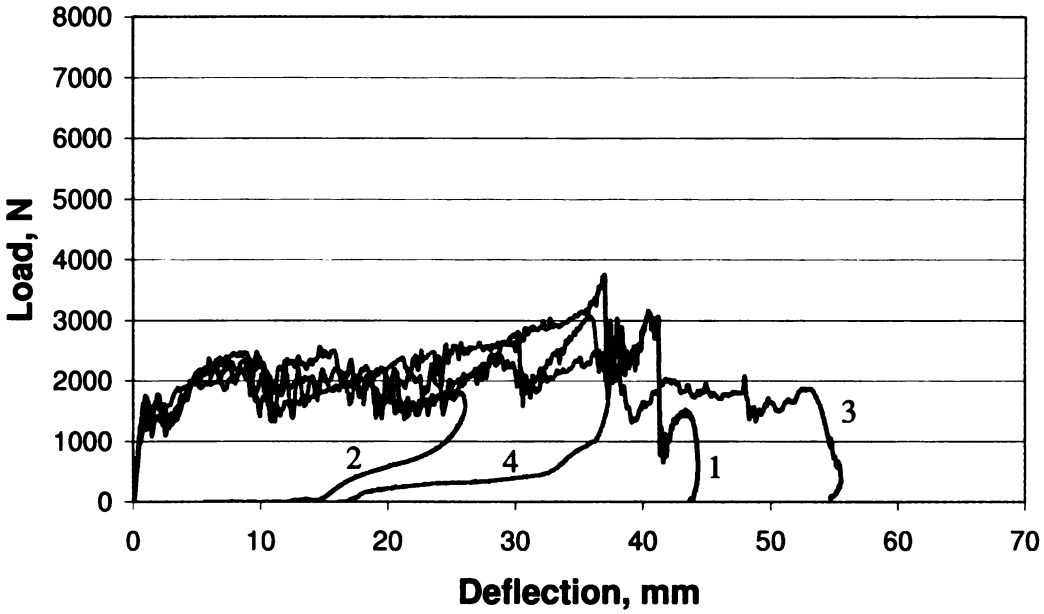

Figure H.1 Bar clamped large arch load-deflection curves.

Table H.1 Bar clamped large arch data.

Specimen #	Stiffness (N/mm)	Peak Load (N)	Deflection @ peak load (mm)	Max. Deflection (mm)	Contact Time (msec)
1	352	3754	37.0	44.3	48.1
2	396	2357	6.6		
3	187	2499	36.6	55.6	48.65
4	372	3062	35.9		
Average	327	2918	29.03	49.93	48.38
Std. Dev.	95	635	14.93	7.95	0.39

Table H.2 Bar clamped large arch energy data.

Specimen #	Impact Energy (J)	Absorbed Energy (J)	Damage
1	94.5	81.3	P
2	44.6	37.5	NP
3	103.1	101.2	P
4	80.5	71.7	NP

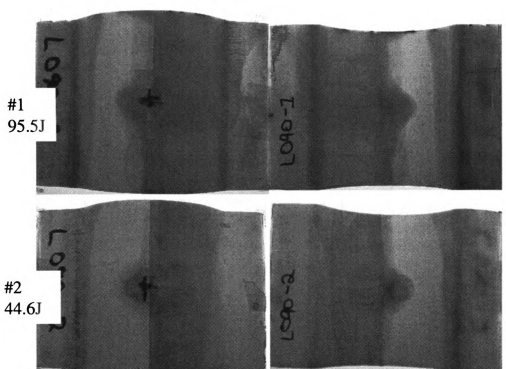

Figure H.2 Bar clamped large arch damaged specimen photos.

Note: Specimen #2 had multiple hits.

APPENDIX I

Small arch with frame clamped boundary condition

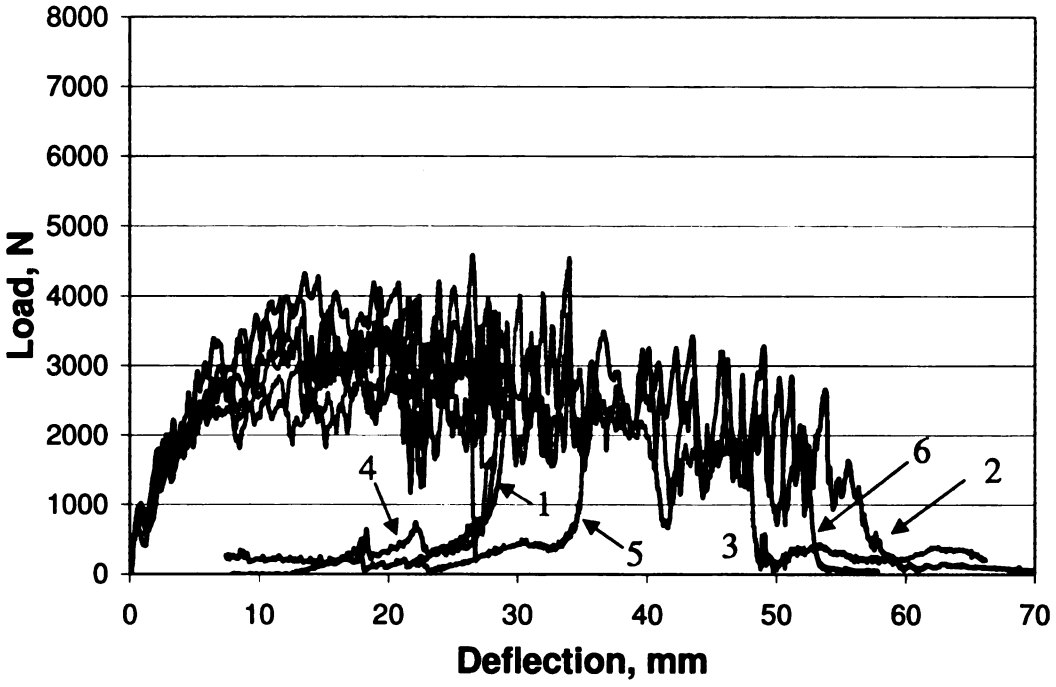

Figure I.1 **Frame clamped small arch load-deflection curves.**

Table I.1 Frame clamped small arch data.

Specimen #	Stiffness (N/mm)	Peak Load (N)	Deflection @ peak load (mm)	Max. Deflection (mm)	Contact Time (msec)
1	329	4102	19.36		
2	230	4051	15.98	60.12	31.00
3	291	3673	13.31	48.97	22.78
4	243	3976	21.56		
5	227	4588	26.50		
6	255	4322	13.53	53.80	31.83
Average	262	4119	18.37	54.30	28.54
Std. Dev.	40	312	5.14	5.59	5.00

Table I.2 Frame clamped small arch energy data.

Specimen #	Impact Energy (J)	Absorbed Energy (J)	Damage
1	81.5	74.1	NP
2	139.0	136.4	P
3	112.4	107.7	P
4	74.0	66.9	NP
5	93.2	87.9	NP
6	130.5	130.2	P

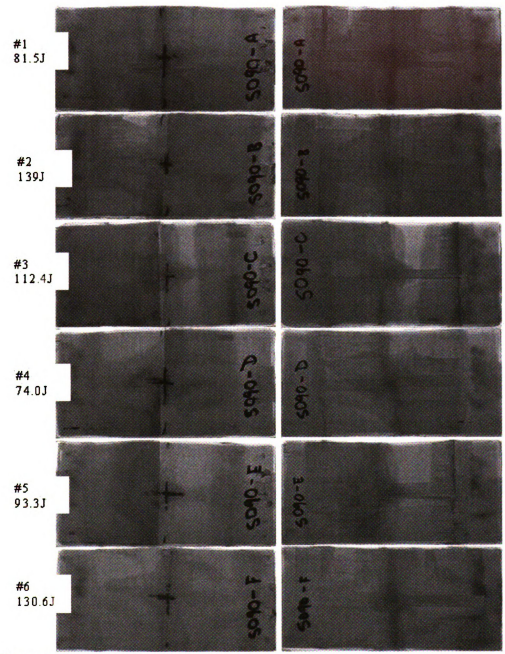

Figure I.2 **Frame clamped small arch damaged specimen photos.**

APPENDIX J

Medium arch with frame clamped boundary condition

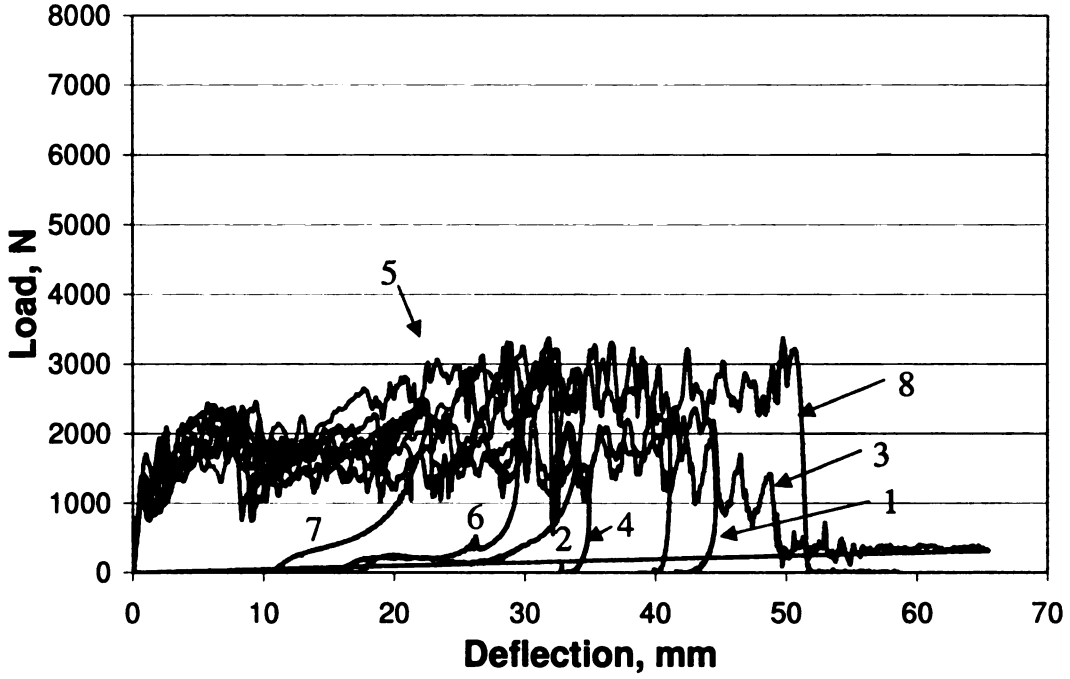

Figure J.1 Frame clamped medium arch load-deflection curves.

Table J.1 Frame clamped medium arch data.

Specimen #	Stiffness (N/mm)	Peak Load (N)	Deflection @ peak load (mm)	Max. Deflection (mm)	Contact Time (msec)
1	194	2382	41.60	44.59	38.53
2	171	3211	32.51		
3	185	2458	9.44	49.67	23.55
4	260	3372	31.85	34.92	32.98
5	194	3308	36.63	41.11	26.78
6	342	2489	22.35		
7	303	2480	22.49		
8	236	3376	49.79	51.70	23.85
Average	236	2884	30.83	44.40	29.14
Std. Dev.	62	466	12.60	6.74	6.47

Table J.2 Frame clamped medium arch energy data.

Specimen #	Impact Energy (J)	Absorbed Energy (J)	Damage
1	71.3	70.4	P
2	61.6	55.2	N
3	83.7	78.9	P
4	68.1	64.3	P
5	95.9	95.8	P
6	54.4	50.5	NP
7	38.3	30.6	NP
8	113.9	113.6	P

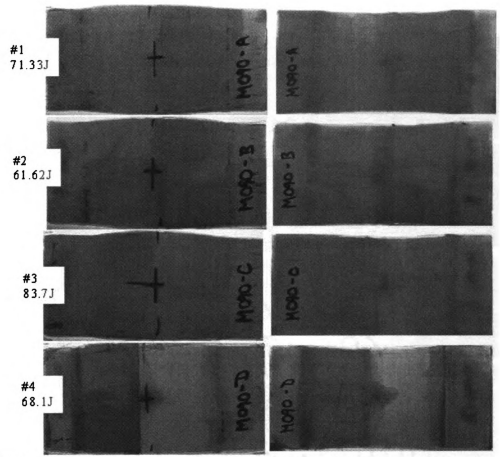

Figure J.2 Frame clamped medium arch damaged specimen photos.

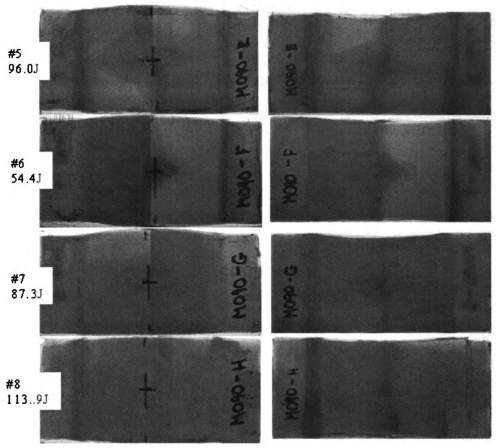

Figure J.3 Frame clamped medium arch damaged specimen photos.

APPENDIX K

Large arch with frame clamped boundary condition

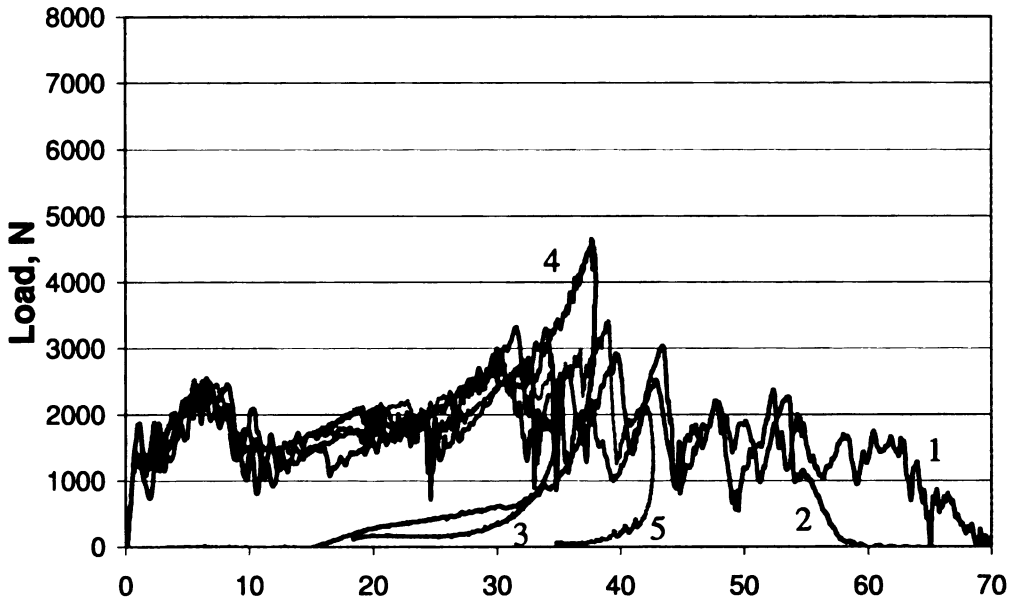

Figure K.1 Frame clamped large arch load-deflection curves.

Table K.1 Frame clamped large arch data.

Specimen #	Stiffness (N/mm)	Peak Load (N)	Deflection @ peak load (mm)	Max. Deflection (mm)	Contact Time (msec)
1	260	3304	33.96	69.22	24.60
2	348	3037	43.42	59.75	36.40
3	258	2815	31.97		
4	239	4649	37.66		
5	296	3417	39.03		
Average	280	3444	37.21	64.49	30.50
Std. Dev.	43	713	4.48	6.70	8.34

Table K.2 Frame clamped large arch data.

Specimen #	Impact Energy (J)	Absorbed Energy (J)	Damage
1	136.3	112.8	P
2	96.8	93.5	P
3	64.3	58.0	NP
4	80.1	66.2	NP
5	87.3	84.6	NP

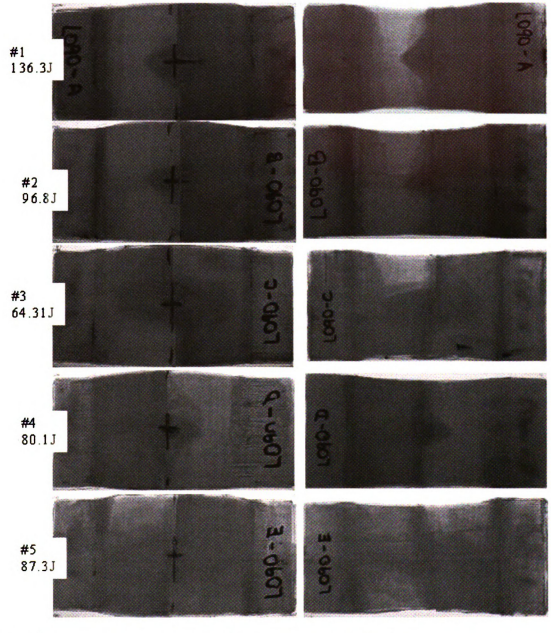

Figure K.2 Frame clamped large arch damaged specimen photos.

APPENDIX L

Small arch with bolted boundary condition

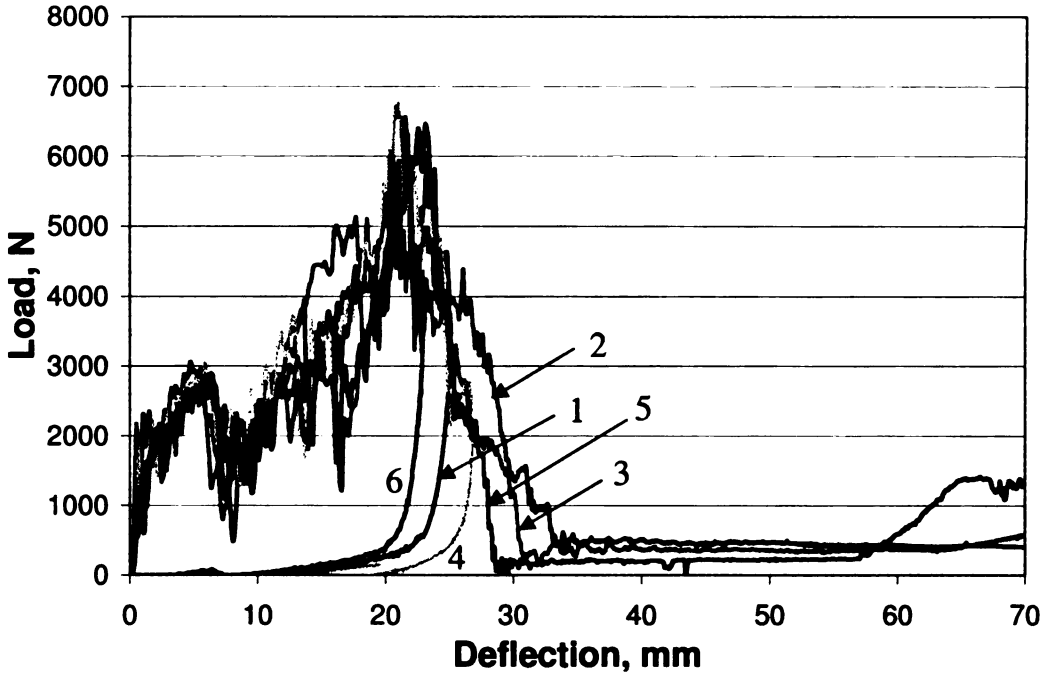

Figure L.1 Bolted small arch load-deflection curves.

Table L.1 Bolted small arch data.

Specimen #	Stiffness (N/mm)	First Peak Load (N)	Second Peak Load (N)	Deflection @ peak load (mm)	Max. Deflection (mm)	Contact Time (msec)
1	299.7	3059	6033	23.3		
2	203	2733	6457	23.1	33.66	11.9
3	251.5	2701	6535	21.5	31.09	11.6
4	327.4	2831	6760	21.0		
5	253.6	2831	5991	20.6	28.6	8.75
6	322.5	2887	5990	22.0		
Average	276.27	2840	6294.30	21.9	31.12	10.75
Std. Dev.	49	127	332.80	1.1	2.53	1.74

Table L.2 Bolted small arch energy data.

Specimen #	Impact Energy (J)	Absorbed Energy (J)	Damage
1	77.8	72.7	NP
2	118.5	105.0	P
3	94.4	79.8	P
4	85.3	83.0	NP
5	109.2	78.4	P
6	63.2	58.0	NP

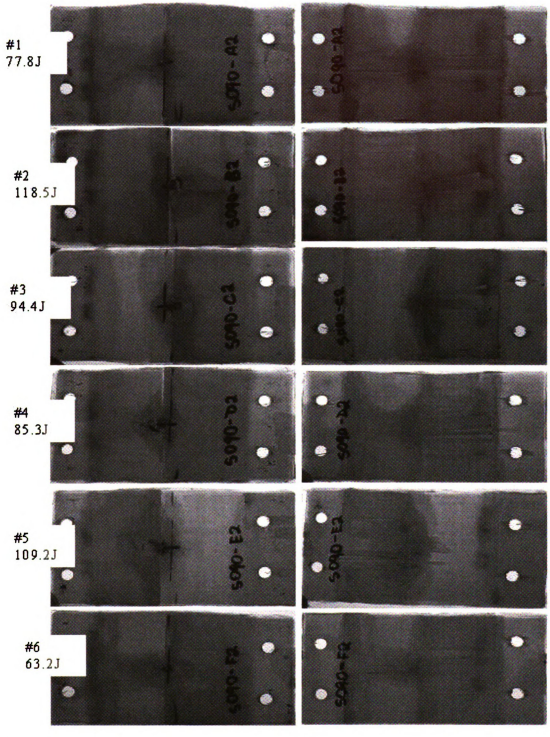

Figure L.2 Bolted small arch damaged specimen photos.

APPENDIX M

Medium arch with bolted boundary condition

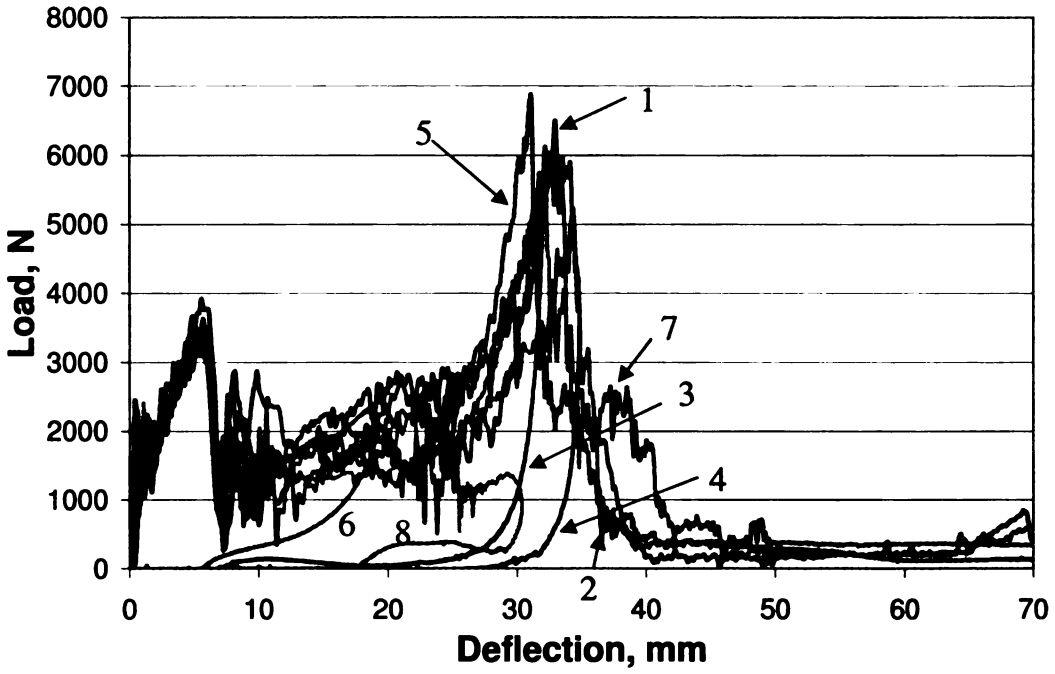

Figure M.1 Bolted medium arch load-deflection curves.

Table M.1 Bolted medium arch data.

Specimen #	Stiffness (N/mm)	First Peak Load (N)	Second Peak Load (N)	Deflection @ peak load (mm)	Max. Deflection (mm)	Contact Time (msec)
1	487.2	3217	6495	32.95	40.74	11.4
2	527	3235	5901	32.23	36.54	15.5
3	586.3	3499	5416	31.90		
4	504	3924	6105	32.19		
5	595	3470	6869	31.07	39.25	12.85
6	749	3378				
7	518	3626	5123	34.30	45.89	14.2
8	640.81	3514				
Average	575.91	3483	5985	32.44	40.61	13.49
Std. Dev.	87.37	227	653	1.09	3.93	1.76

Table M.2 Bolted medium arch energy data.

Specimen #	Impact Energy (J)	Absorbed Energy (J)	Damage
1	130.3	79.5	P
2	86.7	81.2	BITP
3	79.6	71.4	NP
4	94.7	91.3	NP
5	110.5	87.9	P
6	36.0	28.2	NP
7	123.0	87.4	P
8	49.1	45.1	NP

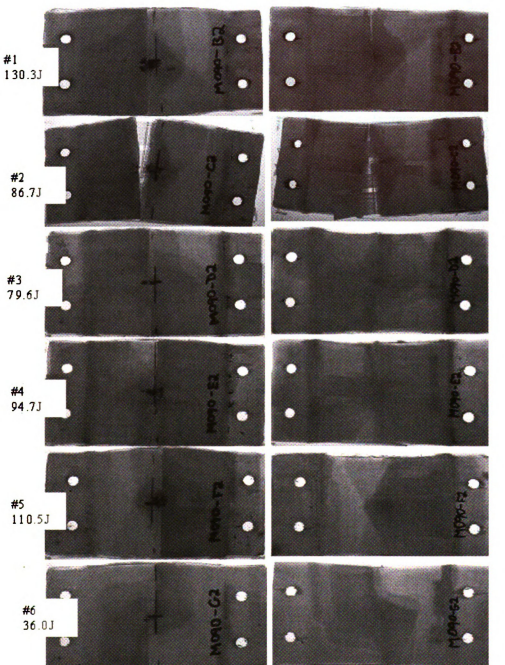

Figure M.2 Bolted medium arch damaged specimen photos.

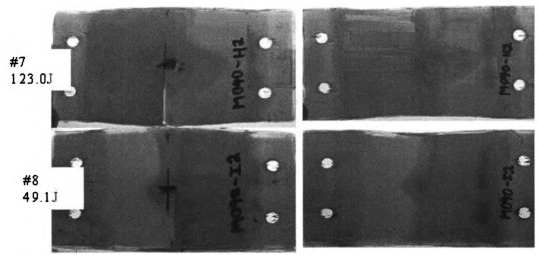

Figure M.2 Bolted medium arch damaged specimen photos.

Note: Specimen #3 had multiple hits.

APPENDIX N

Large arch with bolted boundary condition

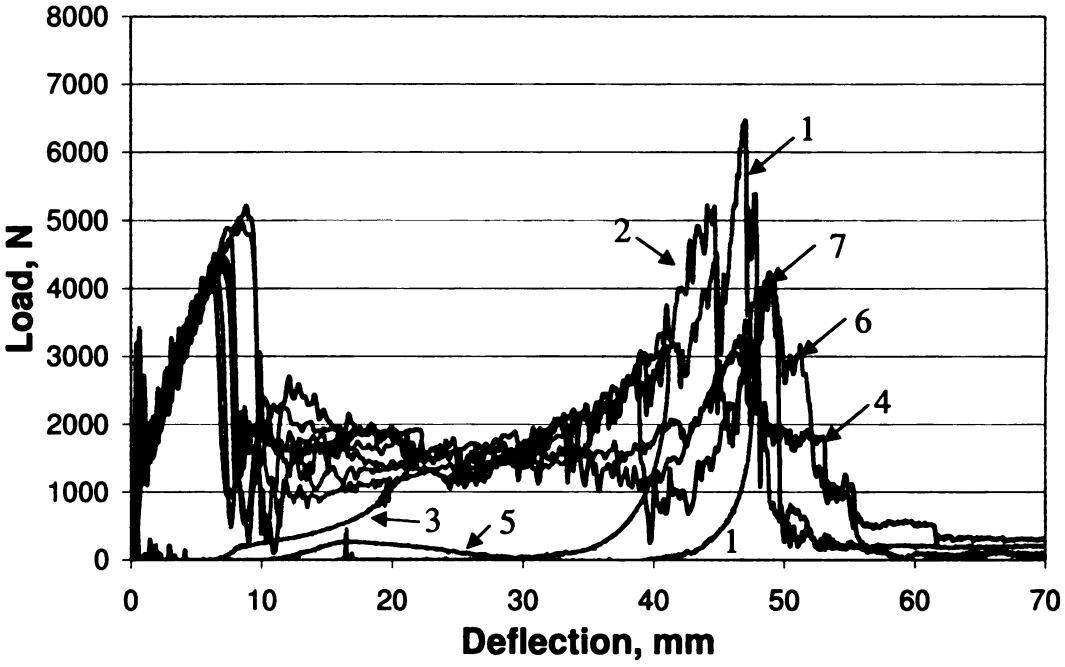

Figure N.1 Bolted large arch load-deflection curves.

Table N.1 Bolted large arch data.

Specimen #	Stiffness (N/mm)	First Peak Load (N)	Second Peak Load (N)	Deflection @ peak load (mm)	Max. Deflection (mm)	Contact Time (msec)
1	560.5	4886	6469.1	47.1		
2	500.27	4425	5208.7	44.1	52.76	19.0
3	554.67	4377				
4	544.47	4457	3373.6	48.0	61.94	25.8
5	607.2	4949				
6	601.2	5211	4229	48.9	59.13	19.9
7	619.5	4454	4229	48.9	49.99	17.4
Average	569.69	4680	4701.89	47.38	55.96	20.51
Std. Dev.	42.12	330	1182.30	1.99	5.53	3.67

Table N.2 Bolted large arch energy data.

Specimen #	Impact Energy (J)	Absorbed Energy (J)	Damage
1	111.6	107.8	NP
2	120.5	108.3	P
3	47.6	38.9	NP
4	116.1	105.0	P
5	80.4	72.8	NP
6	134.5	106.7	P
7	111.7	98.5	BITP

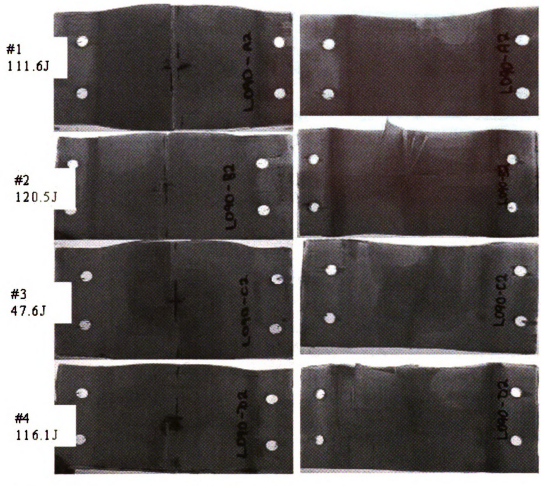

Figure N.2 Bolted large arch damaged specimen photos.

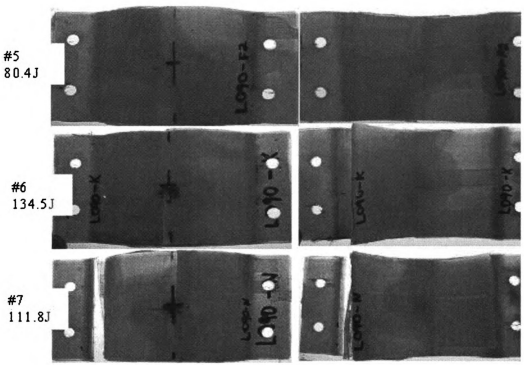

Figure N.3 Bolted large arch damaged specimen photos.

REFERENCES

[1] DeLuca, E., Prifti, J., Betheney, W., Chou, S.C., "Ballistic impact damage of S2-glass-reinforced plastic structural armor," *Composite Science and Technology*, Vol. 58, 1998, pp. 1453-1461.

[2] de Rosset, W.S., "Patterned armor performance evaluation," *International Journal of Impact Engineering*, Vol. 31, 2005, pp. 1223-1234.

[3] Baker, A. , Dutton, S., Kelly, D., ed., "Composite materials for aircraft structures, 2nd Edition.," Reston Virginia, *American Institute of Aeronautics and Astronautics, Inc.*, copyright 2004.

[4] Ambur, D.R., Starnes, H. Jr., "Effect of curvature on the impact damage characteristics and residual strength of composite plates," *39th AIAA/ASME/ASCHE/AHS/ASC Structures, Structural Dynamics, and Materials Conference,* AIAA Paper No. 98-1881, 1998.

[5] Chun, L., Lam, K.Y., "Dynamic analysis of clamped laminated curved panels," *Composite Structures*, Vol. 30, 1995, pp. 389-398.

[6] Cui, Z., Moltschaniwskyj G., Bhattacharyya, D., "Buckling and large deformation behaviour of composite domes compressed between rigid platens," *Composite Structures*, Vol. 66, 2004, pp. 591-599.

[7] Gning, P.B., Tarfaoui, M., Collombet, F., Davies, P., "Prediction of damage in composite cylinders after impact," *Journal of Composite Materials*, Vol. 39, No. 10, 2005, pp. 917-928.

[8] Herszber, I., Weller, T., "Impact damage resistance of buckled carbon/epoxy panels," *Composite Structures*, Vol. 73, 2006, pp. 130-137.

[9] Huang, C.H., Lee Y.J., "Static contact crushing of composite laminated shells," *Composite Structures*, Vol. 63, 2004, pp. 211-217.

[10] Kaczmarek, K., Wisnom, M.R., Jones, M.I., "Edge delamination in curved $(0_4/\pm 45_6)_s$ glass-fibre/epoxy beams loaded in bending,", *Composites Science and Technology, Vol. 58, 1995, pp. 155-161.*

[11] Kim, Y-N, Im, K-H, and Yang, I-Y, "Characterization of Impact Damages and Responses in CFRP Composite Shells," *Materials Science Forum*, Vols. 465-466, 2004, pp. 347-252.

[12] Kistler, L.S., "Experimental Investigation of the impact response of cylindrically curved laminated composite panels," *American Institue of Aeronautics and Astronautics, Inc.*, Vol. 4, 1994, pp. 2292-2297.

[13] Kistler, L.S., "Low Velocity Impact on Curved Laminated Composite Panels," Ph.D. Dissertation, Aerospace Engineering Dept., The University of Michigan, Ann Arbor, MI 1996.

[14] Kistler, L.S., Waas, Anthony M., "On the response of curved laminated panels subjected to transverse impact loads," *International Journal of Solids and Structures*, Vol 36, 1999, pp. 1311-1327.

[15] Krishnamurthy, K.S., Mahajan, P., Mittal, R.K., "Impact response and damage in laminated composite cylindrical shells," *Composite Structures*, Vol. 59, 2003, pp. 15-36.

[16] Leylek, Zafer, Scott, Murray L., Georgiadis, Steve, Thomson, Rodney S., "Computer modeling of impact on curved fibre composite panels," *Composite Structures*, Vol. 47, 1999, pp.789-796.

[17] Nemeth, Michael P., "Nondimensional parameters and equations for buckling of symmetrically laminated thin elastic shallow shells," *NASA Technical Memorandum* 104060, 1991, pp. 1-47.

[18] Shenoi, R.A., Wang, W., "Through-thickness stresses in curved composite laminates and sandwich beams," *Composite Science and Technology*, Vol. 61, 2001, pp. 1501-1512.

[19] Short, G.J., Guild, F.J., Pavier, M.J., "Post-impact compressive strength of curved GFRP laminates," *Composites Part A: applied science and manufacturing*, Vol. 33, 2002, pp. 1487-1495.

[20] Ambur, D.R., Chunchu, P.B., Rose, C.A., Feraboli, P., Jackson, W.C., "Scaling the non-linear impact response of flat and curved anisotropic composite panels," *46th AIAA/ASME/ASCE/AHS/ASC Structures, Dynamics and Materials Conference*, No. 2005-2224, Austin, TX, 2005

[21] Spottswood, S., Palazotto, A.N., "Progressive failure analysis of a composite shell," *Composite Structures*, Vol. 53, 2001, pp. 117-131.

[22] Baucom, J.N., Zikry, M.A., Rajendran, A.M., "Low-velocity impact damage accumulation in woven S2-glass composite systems," *Composite Science and Technology*, Vol. 66, 2006, pp. 1229-1238.

[23] Cheeseman, Bryan A., Bogettie, Travis A., "Ballistic impact into fabric and compliant composite laminates," *Composite Structures*, Vol. 61, 2003, pp. 161-173.

[24] Kirkwood, K.M., Kirkwood, J.E., Lee Y.S., Egres, R.G Jr., Wagner, N.J., Wetzel, E.D., "Yarn pull-out as a mechanism for dissipating ballistic impact energy in Kevlar® KM-2 fabric, Part I: Quasi-static characterization of yarn pull-out," *Textile Research Journal*, Vol. 74, 2004, pp. 920-928.

[25] Huang, X.G., Gillespie, J.W. Jr., Kumar, V., Gavin, L., "Mechanics of integral armor: discontinuous ceramic-cored sandwich structure under tension and shear," *Composite Structures*, Vol. 36, 1996, pp. 81-90.

[26] Jovicic, J., Zavaliangos, A., Ko, F., "Modeling of the ballistic behavior of gradient design composite armors," Composites Part A: applied science and manufacturing, Vol. 31, 2000, pp. 773-784.

[27] www.cymat.com
Cymat Corporation
6320-2 Danville Road,
Mississauga, Ontario, Canada, L5T 2L7

[28] www.instron.com
Instron Corporate Headquarters
825 University Ave.
Norwood, MA 02062-2643

[29] Wardle, Brian L. "Buckling and damage resistance of transversely-loaded composite shells," Ph.D. Dissertation, Dept. of Aeronautics and Astronautics, Massachusetts Institute of Technology, Cambridge, MA, 1998.

[30] Johnson, A.F., Holzapfel, M., "Influence of delamination on impact damage in composite structures," *Composites Science and Technology*, Vol. 66, 2006, pp.807-815.

[31] Ashby, M.F., Evans, A., Fleck, N.A., Gibson, L.J., Hutchinson, J.W., Wadley, H.N.G., "Metal Foams a Design Guide," Butterworth-Heinemann, copyright 2000, pp. 152.